

1 **Historical (1960–2014) lightning and LNO_x trends and their** 2 **controlling factors in a chemistry–climate model**

3 Yanfeng He¹, Kengo Sudo^{1,2}

4 ¹ Graduate School of Environment Studies, Nagoya University, Nagoya, 464-8601, Japan

5 ² Japan Agency for Marine–Earth Science and Technology (JAMSTEC), Yokohama, 237-0061, Japan

6 *Correspondence to:* Yanfeng He (hyf412694462@gmail.com)

7 **Abstract.** Lightning can cause natural hazards that result in human and animal injuries or fatalities, infrastructure destruction,
8 and wildfire ignition. Lightning-produced NO_x (LNO_x), a major NO_x (NO_x=NO+NO₂) source, plays a vital role in atmospheric
9 chemistry and global climate. The Earth has experienced marked global warming and changes in aerosol and aerosol precursor
10 emissions (AeroPEs) since the 1960s. Investigating long-term historical (1960–2014) lightning and LNO_x trends can provide
11 important indicators for all lightning-related phenomena and for LNO_x effects on atmospheric chemistry and global climate.
12 Understanding how global warming and changes in AeroPEs influence historical lightning–LNO_x trends can be helpful in
13 providing a scientific basis for assessing future lightning–LNO_x trends. Moreover, global lightning activities' responses to
14 large volcanic eruptions such as the 1991 Pinatubo eruption are not well elucidated, and are worth exploring. This study
15 employed the widely used cloud top height lightning scheme (CTH scheme) and the newly developed ice-based ECMWF-
16 McCAUL lightning scheme to investigate historical (1960–2014) lightning–LNO_x trends and variations and their influencing
17 factors (global warming, increases in AeroPEs, and Pinatubo eruption) in the framework of the CHASER (MIROC) chemistry–
18 climate model. Results of sensitivity experiments indicate that both lightning schemes simulated almost flat global mean
19 lightning flash rate anomaly trends during 1960–2014 in CHASER-(Mann-Kendall trend test (significance inferred as 5%)
20 shows no trend for the ECMWF-McCAUL scheme, but a 0.03 % yr⁻¹ significant increasing trend is detected for the CTH
21 scheme). Moreover, both lightning schemes suggest that past global warming enhances historical trends of global mean
22 lightning density and global LNO_x emissions in a positive direction (around 0.03% yr⁻¹ or 3% K⁻¹). However, past increases in
23 AeroPEs exert an opposite effect to the lightning–LNO_x trends (-0.07% yr⁻¹ – -0.04% yr⁻¹ for lightning and -0.08% yr⁻¹ – -
24 0.03% yr⁻¹ for LNO_x) when one considers only the aerosol radiative effects in the cumulus convection scheme. Additionally,
25 effects of past global warming and increases in AeroPEs on lightning trends were found to be heterogeneous across different
26 regions when analyzing lightning trends on the global map. Lastly, this report is the first of study results suggesting that global
27 lightning activities were suppressed markedly during the first year after the Pinatubo eruption shown in both lightning schemes
28 (global lightning activities decreased by as much as 18.10% simulated by the ECMWF-McCAUL scheme). Based on simulated
29 suppressed lightning activities after the Pinatubo eruption, findings also indicate that global LNO_x emissions decreased after
30 the 2–3-year Pinatubo eruption (1.99%–8.47% for the annual percentage reduction). Model intercomparisons of lightning flash
31 rate trends and variations between our study (CHASER) and other Coupled Model Intercomparison Project Phase 6 (CMIP6)

32 models indicate great uncertainties in historical (1960–2014) global lightning trend simulations. Such uncertainties must be
33 investigated further.

34 **1 Introduction**

35 Lightning, an extremely energetic natural phenomenon, occurs at every moment somewhere on Earth: its average occurrence
36 frequency is approximately 46 times per second (Cecil et al., 2014). Lightning generation is associated with electric charge
37 separation, which is mainly realized by collisions between graupel and hail and hydrometeors of other types within convective
38 clouds (Lopez, 2016). As a natural hazard, lightning can cause human and animal injuries and fatalities, infrastructure
39 destruction, and wildfire ignition (Cerveny et al., 2017; Cooper and Holle, 2019; Jensen et al., 2022; Veraverbeke et al., 2022).
40 Lightning-produced NO_x (LNO_x) accounts for around 10% of the global tropospheric NO_x ($\text{NO}_x = \text{NO} + \text{NO}_2$) source. It is
41 regarded as the dominant NO_x source in the middle to upper troposphere (Schumann and Huntrieser, 2007; Finney et al.,
42 2016b). Moreover, LNO_x plays a crucially important role in atmospheric chemistry and global climate by affecting the
43 abundances of OH radical, important greenhouse gases (GHGs) such as ozone and methane, and other trace gases (Labrador
44 et al., 2005; Schumann and Huntrieser, 2007; Wild, 2007; Liaskos et al., 2015; Finney et al., 2016a; Murray, 2016; Tost, 2017;
45 He et al., 2022b).

46
47 Reportedly, the lightning flash rate (LFR) is related to the stage of convective cloud development (Williams et al., 1989),
48 Convective Available Potential Energy (CAPE) (Romps et al., 2014), cloud liquid–ice water content (Saunders et al., 1991;
49 Finney et al., 2014) and even to the convective precipitation volume (Goodman et al., 1990; McCaul et al., 2009; Romps et al.,
50 2014). Long-term global warming is associated with changes in the overall temperature and relative humidity profiles in the
51 atmosphere and global convective adjustment (Manabe and Wetherald, 1975; Del Genio et al., 2007), which can strongly affect
52 the lightning-related factors described above. Consequently, long-term global warming can be a fundamentally important
53 factor affecting long-term variations in global lightning activity. Findings from many earlier numerical simulation studies
54 manifest that global lightning activities are sensitive to long-term global warming, with most studies showing 5–16% (average
55 around 10%) increases in global lightning activities per 1 K global warming (Price and Rind, 1994; Zeng et al., 2008; Hui and
56 Hong, 2013; Banerjee et al., 2014; Krause et al., 2014; Romps et al., 2014; Clark et al., 2017). However, other numerical
57 simulation studies such as those using an ice-based lightning scheme or convective mass flux as a proxy to parameterize
58 lightning have yielded opposite results, suggesting that global lightning activity will decrease under long-term global warming
59 (Clark et al., 2017; Finney et al., 2018).

60
61 Aside from long-term global warming, changes in aerosol loading can also be responsible for long-term global lightning
62 activity variations. Aerosols influence lightning activity through aerosol radiative and microphysical effects, but the degree to
63 which the two distinct effects influence regional or global scale lightning activities remains unclear (Yuan et al., 2011; Yang

64 et al., 2013; Tan et al., 2016; Altaratz et al., 2017; Wang et al., 2018; Liu et al., 2020). Further research is needed. It is urgently
65 necessary to elucidate the effects of aerosol radiative and microphysical effects on lightning on a global scale. The aerosol
66 radiative effects indicate that aerosols can heat the atmospheric layer and can cool the Earth's surface by absorbing and
67 scattering solar radiation (Kaufman et al., 2002; Koren et al., 2004, 2008; Li et al., 2017). Thereby, convection and electrical
68 activities are likely to be inhibited (Koren et al., 2004; Yang et al., 2013; Tan et al., 2016). The microphysical effects suggest
69 that by acting as cloud condensation nuclei (CCN) or as ice nuclei, aerosols can reduce the mean size of cloud droplets,
70 consequently suppressing the coalescence of cloud droplets into raindrops. As a result, more liquid water particles are uplifted
71 to higher mixed-phase regions of the troposphere, where they invigorate lightning (Wang et al., 2018; Liu et al., 2020).

72

73 The Earth has experienced a considerable degree of global warming and changes in AeroPEs since the 1960s (Hoesly et al.,
74 2018; Climate at a Glance | National Centers for Environmental Information (NCEI), 2022). However, how historical lightning
75 has trended and how lightning has responded to historical global warming and changes in AeroPEs are not well examined.
76 This topic is worth exploring because historical lightning densities are indicators for all lightning-related phenomena (Price
77 and Rind, 1994). Exploring the historical global LNO_x emission trend is also meaningful because it can indicate the effects of
78 LNO_x emissions on atmospheric chemistry and global climate. Furthermore, investigating the effects of historical global
79 warming and increases in AeroPEs on historical lightning–LNO_x trends can provide a basis for assessing future lightning–
80 LNO_x trends.

81

82 Large-scale volcanic eruptions such as the 1991 Pinatubo eruption inject tremendous amounts of sulfuric gas into the
83 stratosphere, where it converts to H₂SO₄ aerosols. Consequently, the stratospheric aerosols have increased in abundance after
84 the volcanic eruptions. The enhanced stratospheric aerosol layer can cool the Earth's surface heterogeneously and can decrease
85 the total amount of water in the atmosphere (Soden et al., 2002; Boucher, 2015, p.63). The near-global perturbations in the
86 radiative energy balance and meteorological fields caused by such strong volcanic eruptions might influence global lightning
87 activities. If so, there might be ramifications for all lightning-related phenomena. Nevertheless, they remain poorly understood.

88

89 In our earlier work, we developed a new process and ice-based lightning scheme called the ECMWF-McCAUL scheme (He
90 et al., 2022b). This lightning scheme was developed by combining benefits of the lightning scheme used in the European
91 Centre for Medium-Range Weather Forecasts (ECMWF) forecasting system (Lopez, 2016) and those presented in reports by
92 McCaul et al. (McCaul et al., 2009). The ECMWF-McCAUL scheme simulated the best lightning density spatial distributions
93 among four existing lightning schemes when compared against satellite lightning observations (Lightning Imaging Sensor
94 (LIS) and Optical Transient Detector (OTD)) during 2007–2011. The sensitivity of global lightning activity to changes in
95 surface temperature on a decadal timescale was estimated as 10.13% K⁻¹ using the ECMWF-McCAUL scheme (He et al.,
96 2022b), which is close to most past estimates (average around 10% K⁻¹).

97

98 Using a chemistry–climate model CHASER (MIROC) with two lightning schemes (the widely used cloud top height scheme
99 and the ice-based ECMWF-McCAUL scheme), we investigated historical lightning–LNO_x trends quantitatively and
100 ascertained how global warming, increases in AeroPEs, and the Pinatubo eruption respectively influenced them. Using two
101 lightning schemes, we demonstrated the sensitivities of different lightning schemes to historical global warming, increases in
102 AeroPEs, and the Pinatubo eruption.

103

104 Research methods including the model description and experiment setup, are described in Sect. 2. In Sect. 3.1, the simulated
105 historical lightning distributions and trends are validated using LIS/OTD lightning observations. Section 3.2 presents the
106 effects of global warming and increases in AeroPEs on historical lightning–LNO_x trends. In Sect. 3.3, the Pinatubo volcanic
107 eruption effects on historical lightning–LNO_x trends are discussed. Section 3.4 elucidated model intercomparisons of LFR
108 trends and variation between our study (CHASER) and other CMIP6 model outputs. Section 4 presents relevant discussions
109 and conclusions based on these study findings.

110 **2 Method**

111 **2.1 Chemistry–climate model**

112 We used the CHASER (MIROC) global chemistry–climate model (Sudo et al., 2002; Sudo and Akimoto, 2007; Watanabe et
113 al., 2011; Ha et al., 2021) for this study, which incorporated consideration of detailed chemical and physical processes in the
114 troposphere and stratosphere. The CHASER version adopted for this study simulates the distributions of 94 chemical species
115 while reflecting the effects of 269 chemical reactions (58 photolytic, 190 kinetic, and 21 heterogeneous). As processes
116 associated with tropospheric chemistry, Non-Methane Hydrocarbons (NMHC) oxidation and the fundamental chemical cycle
117 of O_x–NO_x–HO_x–CH₄–CO are considered. CHASER simulates stratospheric chemistry involving the Chapman mechanisms
118 and catalytic reactions associated with HO_x, NO_x, ClO_x, and BrO_x. Moreover, it simulates the formation of polar stratospheric
119 clouds (PSCs) and heterogeneous reactions occurring on their surfaces. CHASER is on-line-coupled to MIROC AGCM ver.
120 5.0 (Watanabe et al., 2011), which simulates cumulus convection (Arakawa–Schubert scheme) and grid-scale large-scale
121 condensation to represent cloud and precipitation processes. The radiation flux is calculated using a two-stream k distribution
122 radiation scheme, which considers absorption, scattering, and emissions by aerosol and cloud particles as well as by gaseous
123 species (Sekiguchi and Nakajima, 2008; Goto et al., 2015). The aerosol component in CHASER is coupled with the
124 SPRINTARS aerosol model (Takemura et al., 2009), particularly for simulating primary organic carbon, sea-salt, and dust,
125 which is also based on MIROC. The aerosol radiation effects are considered in both large-scale condensation and cumulus
126 convection schemes, although the aerosol microphysical effects are only reflected in the large-scale condensation scheme.

127

128 This study used a horizontal resolution of T42 (2.8° × 2.8°), with vertical resolution of 36 σ-p hybrid levels from the surface
129 to approximately 50 km. Anthropogenic and biomass burning emissions were obtained from the CMIP6 forcing datasets (van

130 Marle et al., 2017; Hoesly et al., 2018) for 1959–2014 (<https://esgf-node.llnl.gov/search/input4mips/>, last access: 19 September
 131 2022). Interannual variation in biogenic emissions for isoprene, monoterpene, acetone, and methanol were considered using
 132 an off-line simulation by the Vegetation Integrative Simulator for Trace Gases (VISIT) terrestrial ecosystem model (Ito and
 133 Inatomi, 2012). The residual biogenic emissions (ethane, propane, ethylene, propene) used are climatological values derived
 134 from the Model of Emissions of Gases and Aerosols from Nature (MEGAN) modeling system (Guenther et al., 2012).

135

136 The CHASER (MIROC) global chemistry–climate model originally parameterizes lightning with the widely used cloud top
 137 height scheme (Price and Rind, 1992). A newly developed ice-based lightning scheme called the ECMWF-McCAUL here had
 138 been implemented into CHASER (MIROC) (He et al., 2022b). The ECMWF-McCAUL scheme computes LFRs as a function
 139 of CAPE and Q_{Ra} (Q_{Ra} represents the total volumetric amount of cloud ice, graupel, and snow in the charge separation region).
 140 Compared with the cloud top height, a salient advantage of the ECMWF-McCAUL scheme is that it has a direct physical link
 141 with the charging mechanism.

142 2.2 Lightning NO_x emission parameterizations

143 We tested two lightning schemes for this study. The first lightning scheme is the widely used cloud top height (CTH) scheme
 144 (Price and Rind, 1992), which was used originally in CHASER (MIROC). This lightning scheme uses the following equations
 145 to calculate LFR.

$$146 F_l = 3.44 \times 10^{-5} H^{4.9} \quad (1)$$

$$147 F_o = 6.2 \times 10^{-4} H^{1.73} \quad (2)$$

148 Therein, F represents the total flash frequency (fl. min⁻¹), H stands for the cloud-top height (km), and subscripts l and o
 149 respectively denote the land and ocean (Price and Rind, 1992). Actually, we realize the CTH scheme in CHASER using the
 150 following equations (Eq. (3) and Eq. (4)) (Sudo et al., 2002). Each model layer’s cumulus cloud fractions are used to
 151 weight the calculated lightning densities from that layer in the CTH scheme.

$$152 F_l = \sum_{i=1}^{n=36} adj_factor \times Cu_CF_i \times (H_i - H_{surface})^{4.9} \quad (3)$$

$$153 F_o = \sum_{i=1}^{n=36} adj_factor \times Cu_CF_i \times (H_i - H_{surface})^{1.73} \quad (4)$$

154 In those equations, i represents the model layer index. In addition, adj_factor represents adjustment factors that differ for
 155 different model layers and model grids. Cu_CF_i symbolizes the cumulus cloud fraction at model layer i . H_i and $H_{surface}$
 156 respectively denote the altitude of model layer i and the altitude of the model’s surface layer.

157

158 The second lightning scheme used for this study is a newly developed one named the ECMWF-McCAUL scheme (He et al.,
 159 2022b), which is based on the original ECMWF scheme and findings reported by McCaul et al. (2009). The ECMWF-
 160 McCAUL scheme calculates LFRs as a function of CAPE (m² s⁻²) and Q_{Ra} (Q_{Ra} symbolizes the total volumetric amount of
 161 cloud ice, graupel, and snow in the charge separation region) as

162 $f_l = \alpha_l Q_{Ra} CAPE^{1.3}$ (5)

163 $f_o = \alpha_o Q_{Ra} CAPE^{1.3}$ (6)

164 where f_l and f_o respectively symbolize the total flash density (fl. m⁻² s⁻¹) over land and ocean. In addition, α_l and α_o are
 165 constants (fl. s^{1.6} kg⁻¹ m^{-2.6}) determined after calibration against LIS/OTD climatology, respectively, for land and ocean. For
 166 this study, α_l and α_o are set respectively as 2.67×10^{-16} and 1.68×10^{-17} . In the charge separation region (from 0° to -25°C
 167 isotherm), Q_{Ra} (kg m⁻²) is expressed as a proxy for the charging rate because of collisions between graupel and hydrometeors
 168 of other types (McCaul et al., 2009). Moreover, Q_{Ra} represents the total volumetric amount of hydrometeors of three kinds
 169 (graupel, snow, and cloud ice) within the charge separation region, calculated as

170 $Q_{Ra} = \int_{z_0}^{z-25} (q_{graup} + q_{snow} + q_{ice}) \bar{\rho} dz,$ (7)

171 where q_{graup} , q_{snow} , and q_{ice} respectively represent the mass mixing ratios (kg kg⁻¹) of graupel, snow, and cloud ice. In
 172 addition, q_{ice} was diagnosed using Arakawa–Schubert cumulus parameterization. Then, q_{graup} and q_{snow} were computed at
 173 each vertical level of the model using the following equations.

174 $q_{graup} = \beta \frac{P_f}{\bar{\rho} V_{graup}}$ (8)

175 $q_{snow} = (1 - \beta) \frac{P_f}{\bar{\rho} V_{snow}}$ (9)

176 In those equations, P_f represents the vertical profile of the frozen precipitation convective flux (kg m⁻² s⁻¹), $\bar{\rho}$ denotes the air
 177 density (kg m⁻³), and V_{graup} and V_{snow} respectively express the typical fall speeds for graupel and snow set to 3.1 and 0.5
 178 m s⁻¹ for this study. For land, the dimensionless coefficient β is set as 0.7, whereas it is set to 0.45 for oceans to consider the
 179 observed lower graupel content over the oceans.

180

181 Based on the cold cloud depth, a fourth-order polynomial (equation 10) is used to calculate the proportion of total flashes that
 182 are cloud-to-ground (p). An earlier report of the literature describes the method (Price and Rind, 1993).

183 $p = \frac{1}{64.9 - 36.54D + 7.493D^2 - 0.648D^3 + 0.021D^4}$ (10)

184 The depth of the cloud above the 0°C isotherms is represented by D (km) in that equation.

185

186 According to recent studies, the intra-cloud (IC) lightning flashes are as efficient as cloud-to-ground (CG) lightning flashes
 187 at producing NO_x. The lightning NO_x production efficiency is estimated as 100–400 mol per flash (Ridley et al., 2005;
 188 Cooray et al., 2009; Ott et al., 2010; Allen et al., 2019). The LNO_x production efficiencies for IC and CG are therefore set to
 189 the same value (250 mol per flash) in CHASER, which is the median of the commonly cited range of 100–400 mol per flash.
 190 Therefore, in this study, the distinctions between IC and CG do not affect the distribution or magnitude of LNO_x emissions.
 191 It is noteworthy that marked uncertainties are involved in ascertaining the LNO_x production efficiency (Allen et al., 2019;
 192 Bucselá et al., 2019). The choice of a different LNO_x production efficiency might affect the simulation of LNO_x emissions.
 193 Further research must be undertaken to implement and validate a more sophisticated parameterization of LNO_x production

194 efficiency in chemistry–climate models. The calculated total column LNO_x for each grid was distributed into each model
195 layer based on a prescribed “backward C-shaped” LNO_x vertical profile (Ott et al., 2010).

196 **2.3 Lightning observation data for model evaluation**

197 We used LIS/OTD gridded climatology datasets for this study, consisting of climatologies of total LFRs observed using the
198 Lightning Imaging Sensor (LIS) and Optical Transient Detector (OTD). The OTD aboard the MicroLab-1 satellite and LIS
199 aboard the Tropical Rainfall Measuring Mission (TRMM) satellite (Cecil et al., 2014). Both sensors detected lightning by
200 monitoring pulses of illumination produced by lightning in the 777.4 nm atomic oxygen multiplet above background levels.
201 In low Earth orbit, both sensors viewed Earth locations for approximately 3 min during the pass of the OTD or 1.5 min during
202 passing of the LIS. Each day, OTD and LIS respectively orbited the globe 14 times and 16 times. OTD observed data between
203 +75 and -75° latitude during May 1995 – March 2000, whereas LIS collected data between +38 and -38° latitude during
204 January 1998 – April 2015. This study uses the LIS/OTD 2.5 Degree Low Resolution Time Series (LRTS), which provides
205 daily LFRs on a 2.5° regular latitude–longitude grid for May 1995 – April 2015.

206 **2.4 CMIP6 model outputs for model comparison**

207 For the comparison of different model outputs from our study (CHASER) and other Earth system models or chemistry–climate
208 models, we used LFR and surface temperature data from the CMIP6 CMIP Historical experiments from CESM2-WACCM
209 (Danabasoglu, 2019), GISS-E2-1-G (Kelley et al., 2020), and UKESM1-0-LL (Tang et al., 2019). CESM2-WACCM uses the
210 Community Earth System Model ver. 2 (Danabasoglu et al., 2020). The CESM2 is an open-source fully coupled Earth system
211 model. The Whole Atmosphere Community Climate Model ver. 6 (WACCM6) is the atmospheric component coupled to the
212 other components in CESM2. The GISS-E2-1-G is the NASA Goddard Institute for Space Studies (GISS) chemistry–climate
213 model version E2.1 based on the GISS Ocean v1 (G01) model (Miller et al., 2014; Kelley et al., 2020). The UKESM1-0-LL
214 is the UK's Earth system model, details of which were described by Sellar et al. (2019). We used 3 ensembles from CESM2-
215 WACCM, 9 ensembles from GISS-E2-1-G, and 18 ensembles from UKESM1-0-LL. Table S1 presents all the ensemble
216 members used for this study.

217 **2.5 Experiment setup**

218 We have conducted six sets of experiments with each set of experiments conducted using both the ECMWF-McCAUL
219 (abbreviated as F1) and CTH (abbreviated as F2) schemes. Table 1 presents the major settings of all experiments with the
220 relative explanations of those settings. STD-F1/F2 are standard experiments with the simulation period of 1959–2014. They
221 are intended to reproduce the historical trends of lightning and LNO_x. Climate1959-F1/F2 are experiments that keep the climate
222 simulations fixed to 1959 to derive the effects of global warming on historical lightning trends. ClimateAero1959-F1/F2 are
223 intended to reflect the conditions with climate simulations and aerosol and aerosol precursor (BC, OC, NO_x, SO₂) emissions
224 fixed to 1959. The Aero1959-F1/F2 experiments are the same as the STD-F1/F2 experiments, except for the AeroPEs fixed to

225 1959. The fifth set of experiments (Volca-off-F1/F2) was intended to exclude the influences of the Pinatubo volcanic eruption
226 to compare to the STD-F1/F2 and to evaluate the Pinatubo eruption effects on historical lightning–LNO_x trends and variation.
227

228 We simulate volcanic aerosol forcing by considering the prescribed stratospheric aerosol extinction in the radiation scheme.
229 We used the NASA Goddard Institute for Space Studies (GISS) (Sato et al., 1993) and Chemistry–Climate Model Initiative
230 (CCMI) (Arfeuille et al., 2013) stratospheric aerosol dataset as the stratospheric aerosol climate data. The NASA GISS dataset
231 includes monthly zonal-mean stratospheric aerosol optical thickness in four spectral bands. The CCMI dataset for CHASER
232 includes monthly zonal-mean stratospheric aerosol extinction coefficients in 20 spectral bands. To remove the volcanic
233 perturbation while maintaining the stratospheric background aerosol in the Volca-off-F1/F2, we used the following equation
234 to process the Stratospheric Aerosol Climatology (SAC) during June 1991 – May 1996.

$$235 \mathbf{SAC}_{no_pinatubo} = \begin{cases} \mathbf{SAC}_{background}, & |\mathbf{SAC}_{raw} - \mathbf{SAC}_{background}| > 1.96\sigma, \\ \mathbf{SAC}_{raw}, & |\mathbf{SAC}_{raw} - \mathbf{SAC}_{background}| \leq 1.96\sigma \end{cases} \quad (11)$$

236 In that equation, $\mathbf{SAC}_{no_pinatubo}$ denotes the stratospheric aerosol climatological data as input data for Volca-off-F1/F2
237 experiments, $\mathbf{SAC}_{background}$ represents the stratospheric background aerosol climatological data (For this study,
238 $\mathbf{SAC}_{background}$ is the corresponding temporal averaged values of the NASA GISS and CCMI stratospheric aerosol
239 dataset during June 1986 – May 1991 and June 1996 – May 2001, when the time is close to the eruption and the stratosphere
240 was less affected by volcanic eruptions). \mathbf{SAC}_{raw} stands for the original values of NASA GISS and CCMI stratospheric
241 aerosol dataset during June 1991 – May 1996. Moreover, σ symbolizes the standard deviations of stratospheric
242 background aerosol climate data (For this study, σ are the corresponding standard deviations of NASA GISS and CCMI
243 stratospheric aerosol dataset during June 1986 – May 1991 and June 1996 – May 2001). As displayed in Eq. (11), when
244 the absolute differences between \mathbf{SAC}_{raw} and $\mathbf{SAC}_{background}$ are larger than 1.96σ , we replace the original values (June
245 1991 – May 1996) of the SAC with the temporal averaged values of the NASA GISS and CCMI dataset during June 1986
246 – May 1991 and June 1996 – May 2001. When the absolute differences between \mathbf{SAC}_{raw} and $\mathbf{SAC}_{background}$ are equal to
247 or smaller than 1.96σ , we still use the original values (June 1991 – May 1996) of the SAC for the Volca-off experiments.
248 The value of 1.96σ corresponds to the 95% confidence interval, which can remove the Pinatubo perturbation sufficiently
249 but which can maintain the background level of stratospheric aerosol during June 1991 – May 1996. Furthermore, the
250 influences of the Pinatubo eruption affected the HadISST SSTs/sea ice fields. To remove the Pinatubo eruption's
251 influences on the SSTs/sea ice fields from the Volca-off experiments also, we replaced the 1991-06 – 1995-05 SSTs/sea
252 ice data with HadISST SSTs/sea ice climatological data during 1985–1990 when conducting the Volca-off experiments.
253 The 1985–1990 period was chosen because it is approximately the period of 1991-06 – 1995-05 and because the SSTs/sea
254 ice fields were less affected by volcanic activity during 1985–1990.

255

256 All the experiments calculate the LNO_x emissions rates interactively by LNO_x emission parameterizations except STD-
 257 rVolcaoff experiments. The STD-rVolcaoff experiments are the same as the STD experiments except for reading the
 258 daily LNO_x emission rates calculated from the Volca-off experiments. The STD-rVolcaoff experiments are conducted
 259 for comparison with STD experiments to elucidate the effects of LNO_x emissions changes caused by the Pinatubo
 260 eruption on atmospheric chemistry (typically methane lifetime).

261 **Table 1: All experiments conducted for this study**

Name of experiment	Period	Climate (SSTs, sea ice, GHGs) ^a	Anthropogenic and biomass burning emissions	Biogenic emissions	Stratospheric aerosol climatology
STD-F1/F2 ^b	1959–2014	1959–2014	CMIP6 1959–2014		NASA GISS and CCM1 stratospheric aerosol dataset ^c
Climate1959-F1/F2	1959–2014	Fixed to 1959 ^d	CMIP6 1959–2014		As above
ClimateAero1959-F1/F2	1959–2014	Fixed to 1959	AeroPEs fixed to 1959 ^e	VISIT and MEGAN ^f	As above
Aero1959-F1/F2	1959–2014	1959–2014	AeroPEs fixed to 1959		As above
Volca-off-F1/F2	1990–1999	1990–1999 ^g	CMIP6 1990–1999		Same dataset with volcanic perturbation removed
STD-rVolcaoff-F1/F2	1990–1999	All settings are the same as those used for STD experiment except for reading of the daily LNO _x emission rates calculated from the Volca-off experiments			

262 ^a For the model simulations, the climate is simulated by the prescribed SSTs/sea ice fields and the prescribed varying
 263 concentrations of GHGs (CO₂, N₂O, methane, chlorofluorocarbons – CFCs – and hydrochlorofluorocarbons – HCFCs) used
 264 only in the radiation scheme. The SSTs/sea ice fields are obtained from the HadISST dataset (Rayner et al., 2003). The
 265 prescribed GHGs concentrations are derived from CMIP6 forcing datasets (Meinshausen et al., 2017).

266 ^b We use “F1” to stand for the ECMWF-McCAUL scheme; “F2” represents the CTH scheme.

267 ^c Stratospheric aerosol radiative forcing is simulated using the prescribed stratospheric aerosol extinction, which is obtained
 268 from the NASA GISS (Sato et al., 1993) and CCM1 (Arfeuille et al., 2013) stratospheric aerosol dataset.

269 ^d The climate is fixed to 1959 for the whole simulation period using the 1959 SSTs/sea ice field and GHG concentrations
 270 during the simulation period.

271 ^e Aerosol (BC, OC) and aerosol precursor (NO_x, SO₂) emissions (anthropogenic + biomass burning) are fixed to 1959
272 throughout the simulation period.

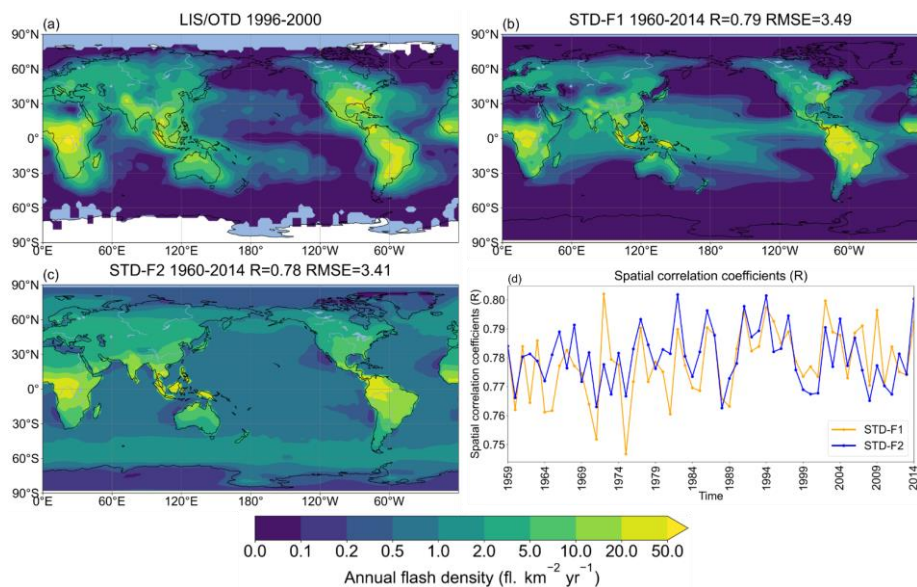
273 ^f Several biogenic emissions are interannually varying, including isoprene, monoterpenes, acetone, and methanol, which were
274 calculated using an off-line simulation using the Vegetation Integrative Simulator for Trace Gases (VISIT) terrestrial
275 ecosystem model (Ito and Inatomi, 2012). Some other reactive biogenic VOCs (ethane, propane, ethylene, propene) used are
276 climatological data derived from the Model of Emissions of Gases and Aerosols from Nature (MEGAN) modeling system
277 (Guenther et al., 2012).

278 ^g Here the 1991-06 – 1995-05 SSTs/sea ice data were replaced with HadISST SSTs/sea ice climatological data during
279 1985–1990.

280 3 Results and Discussion

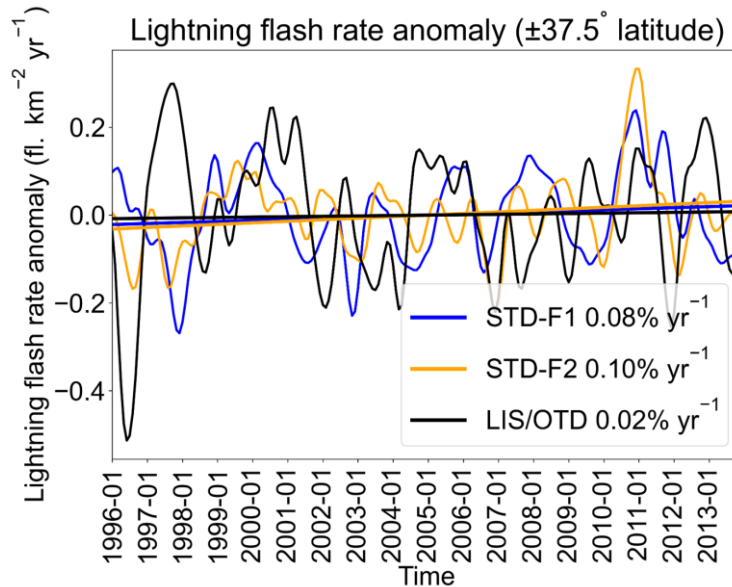
281 3.1 Validation of the simulated historical lightning distribution and trend

282 To increase the credibility of the conclusions obtained based only on the numerical simulations, the model calculations must
283 be evaluated using observational data. We used the LIS/OTD observations to evaluate the spatial and temporal distribution
284 and historical lightning trends simulated by CHASER (MIROC). Figures 1a–1c show the annual mean spatial distributions of
285 lightning observed by LIS/OTD and from model simulations using the ECMWF-McCAUL and CTH schemes. Both the
286 ECMWF-McCAUL and CTH schemes generally captured the hotspots of lightning (Central Africa, Maritime Continent, South
287 America), with strong spatial correlations between observations and model simulations ($R > 0.75$), even the lightning
288 distributions were not well captured over the ocean. Figure 1d exhibits strong spatial correlation between observations and
289 simulation results maintained throughout the simulation period (1959–2014).



290

291 **Figure 1: Annual mean lightning flash densities from (a) LIS/OTD satellite observations spanning 1996–2000, (b) the STD**
 292 **experiment (1960–2014) with the ECMWF-McCAUL scheme used, (c) the STD experiment (1960–2014) with the CTH scheme used.**
 293 **R and RMSE shown in the titles of panels (b) and (c) are calculated between panels (b)–(c) and (a). Panel (d) presents the spatial**
 294 **correlation coefficients between modeled spatial lightning distribution of each year and LIS/OTD lightning climatologies during**
 295 **1996–2000.**



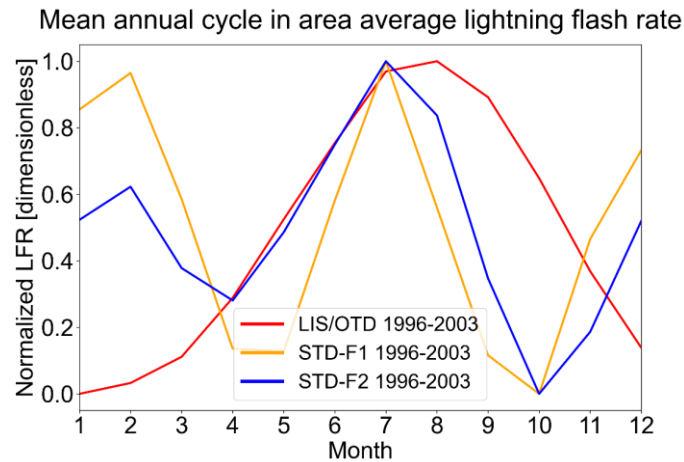
296
 297 **Figure 2: LFR anomalies of 1996–2013 within $\pm 37.5^\circ$ latitude obtained from two numerical experiments (STD-F1/F2) and LIS/OTD**
 298 **satellite observations. Curves represent the monthly time-series data of the $\pm 37.5^\circ$ latitude mean LFR anomalies with the 1-D**
 299 **Gaussian (Denoising) filter applied. Lines are the fitting curves of the monthly time-series data of the $\pm 37.5^\circ$ latitude mean LFR**
 300 **anomalies. Trends of the LFR anomalies in $\% \text{ yr}^{-1}$ are also presented in the legends.**

301
 302 **Table 2: A statistical summary of the trends shown in Fig. 2 by Mann–Kendall rank statistic and Sen’s slope estimator. The monthly**
 303 **time-series data of the $\pm 37.5^\circ$ latitude mean LFR anomalies were estimated by Mann–Kendall rank statistic and Sen’s slope estimator.**
 304 **The column “Trend” shows whether these are significant trends with the significance set as 5%, as well as the percentage trends in $\%$**
 305 **yr^{-1} estimated by linear regression. The “ p -value” is calculated during Mann-Kendall trend test. “Slope” shows Sen’s slope of trend.**
 306 **Q_{\min} and Q_{\max} respectively denote the lower and upper limits of the 95% confidence interval of Sen’s slope.**

<u>Experiment/dataset</u>	<u>Trend</u>	<u>p-value</u>	<u>Slope</u>	<u>Q_{\min}</u>	<u>Q_{\max}</u>
<u>STD-F1</u>	<u>No trend, 0.08 % yr^{-1}</u>	<u>$p > 0.05$</u>	<u>0.0001</u>	<u>-0.0003</u>	<u>0.0005</u>
<u>STD-F2</u>	<u>No trend, 0.10 % yr^{-1}</u>	<u>$p > 0.05$</u>	<u>0.0003</u>	<u>0.0</u>	<u>0.0006</u>
<u>LIS/OTD</u>	<u>No trend, 0.02 % yr^{-1}</u>	<u>$p > 0.05$</u>	<u>-0.0001</u>	<u>-0.0006</u>	<u>0.0004</u>

307
 308 The LIS/OTD observations are also used to evaluate historical lightning trends simulated by CHASER (MIROC). We
 309 examined the $\pm 37.5^\circ$ latitude mean LFR anomaly (1996–2013) calculated from LIS/OTD observations and STD-F1/F2

310 numerical experiments (Fig. 2 and Table 2). We also note some missing values within the $\pm 37.5^\circ$ latitude in LIS/OTD
 311 observations. To constrain the comparisons between observations and simulations as like-for-like, when we encounter a
 312 missing value in the LIS/OTD observations during spatial averaging, we also treat the CHASER simulated value at the same
 313 location as a missing value. As displayed in Fig. 2, even when the we would not necessarily expect that interannual variations
 314 of the LFR anomaly sometimes differ between observations can be captured, because meteorological nudging was not applied
 315 and simulations the simulated LFRs were only controlled by the prescribed SSTs/sea ice data. Nevertheless, the overall trends
 316 of LFR anomaly simulated using both schemes well-matched the LIS/OTD observations, as portrayed in Fig. 2. We further
 317 investigated the trends shown in Fig. 2 by Mann–Kendall rank statistic and Sen’s slope estimator and the statistical summary
 318 is displayed in Table 2 (T. et al., 2002; Hussain and Mahmud, 2019). Neither the LFR anomaly (within $\pm 37.5^\circ$ latitude) derived
 319 from LIS/OTD observations nor simulations show a significant trend for 1996–2013 using the Mann–Kendall rank statistic
 320 test (significance inferred for 5%). The global LFR anomaly during 1993–2013 obtained from simulations (STD-F1/F2) also
 321 shows no significant trend, which is consistent with the Schuman Resonance (SR) intensity observations (1993–2013) at Rhode
 322 Island, USA (Earle Williams, 2022). However, the SR observations in Rhode Island (USA) exclude consideration of the
 323 influences of solar cycles, which makes it less appropriate for lightning trend evaluation.



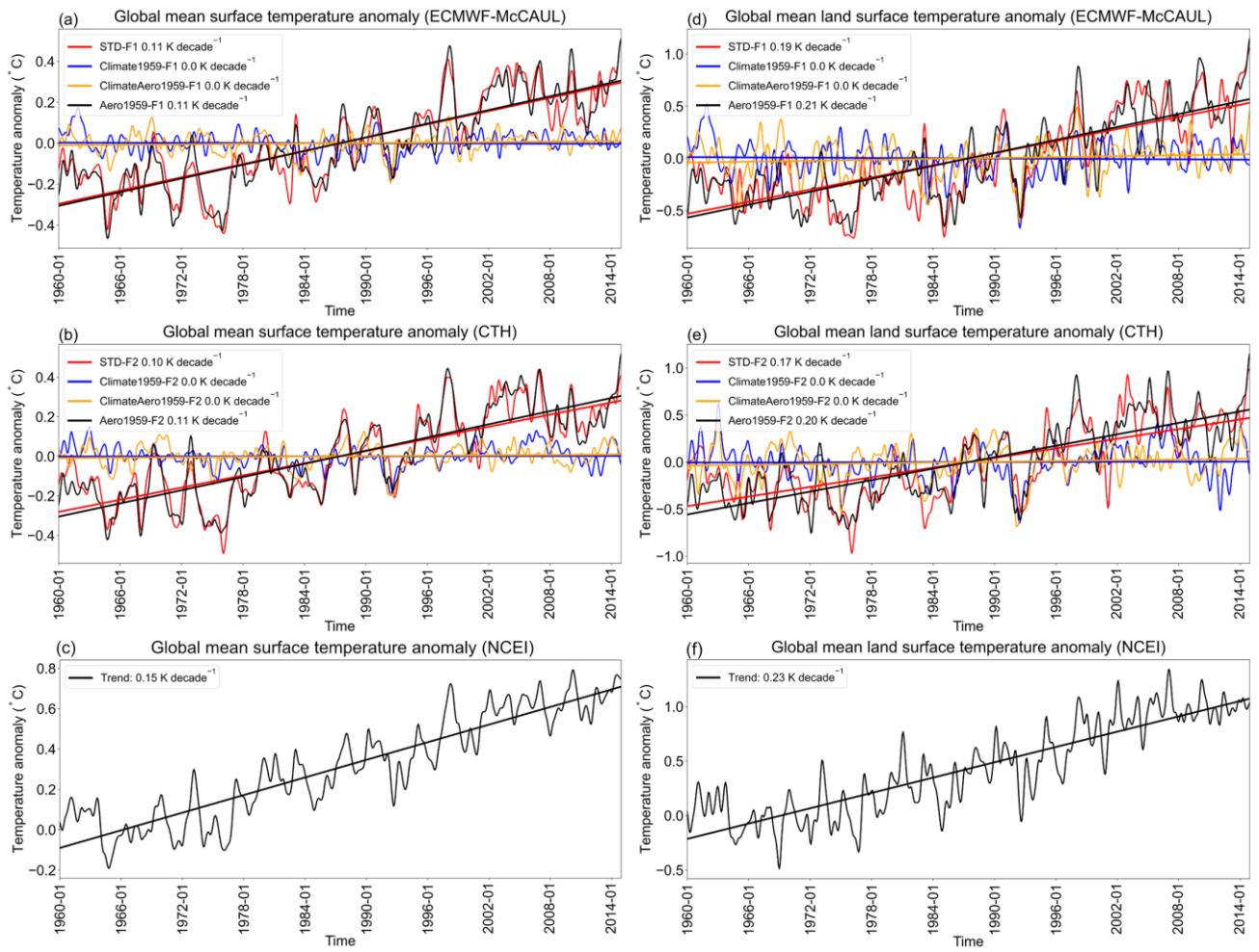
324
 325 **Figure 3: Mean annual cycle in area average LFR during 1996–2003. The area average was taken over the grid cells where valid**
 326 **LIS/OTD lightning observations exist. LFR is normalized by min-max normalization.**

327
 328 We further investigated the seasonal variabilities of simulated LFR and compared them against LIS/OTD observations. The
 329 results are depicted in Fig. 3. Both the CTH and ECMWF-McCAUL schemes captured the peak during JJA, but the
 330 overestimation of LFR by F1/F2 during DJF is also noticeable. Figure S1 presents comparison of the LFR global distribution
 331 in different seasons during 1996–2003 from LIS/OTD lightning observations and STD experiment outputs. Generally,
 332 CHASER well-captured the spatial distribution of LFR in all four seasons when compared against LIS/OTD observations. The
 333 spatial correlation coefficients (R) between observations and simulations are highest ($R=0.80$ for both lightning schemes) in
 334 DJF, indicating CHASER’s considerable capability to reproduce the LFR spatial distribution in DJF. As displayed in the first

335 row of Fig. S1, the overestimation of LFR by F1/F2 during DJF is primarily attributable to the overestimation of LFR within
336 the Maritime Continent and South America, but this might also be attributable to the underestimation of LFR by LIS/OTD
337 within these two regions. It is believed that the LIS/OTD lightning detection efficiency is highly sensitive to the characteristic
338 of convective clouds (cloud albedo, cloud optical thickness, etc.) (Boccippio et al., 2002; Cecil et al., 2014). High cloud albedo
339 and cloud optical thickness might engender the underestimation of LFR by LIS/OTD. It is also noteworthy that the seasonal
340 variation and long-term trend of global lightning are strongly influenced by distinct different factors. The seasonal variation
341 of global lightning activities is most strongly affected by the 23° obliquity of Earth’s orbit and the asymmetric distribution of
342 the continent between the Northern and Southern hemispheres. However, the long-term global lightning trend we investigated
343 for this study is controlled mainly by climate forcings such as aerosols and GHGs. To minimize the effects of LFR seasonal
344 variation on our study’s results, we deseasonalized the results shown in all figures and tables by calculating their anomaly
345 based on raw data. The validation described above and the deseasonalization of our study’s results justified that the LFR
346 seasonal variation (and the uncertainties in the simulation of LFR seasonal variation) in our study has a limited effect on these
347 study results.

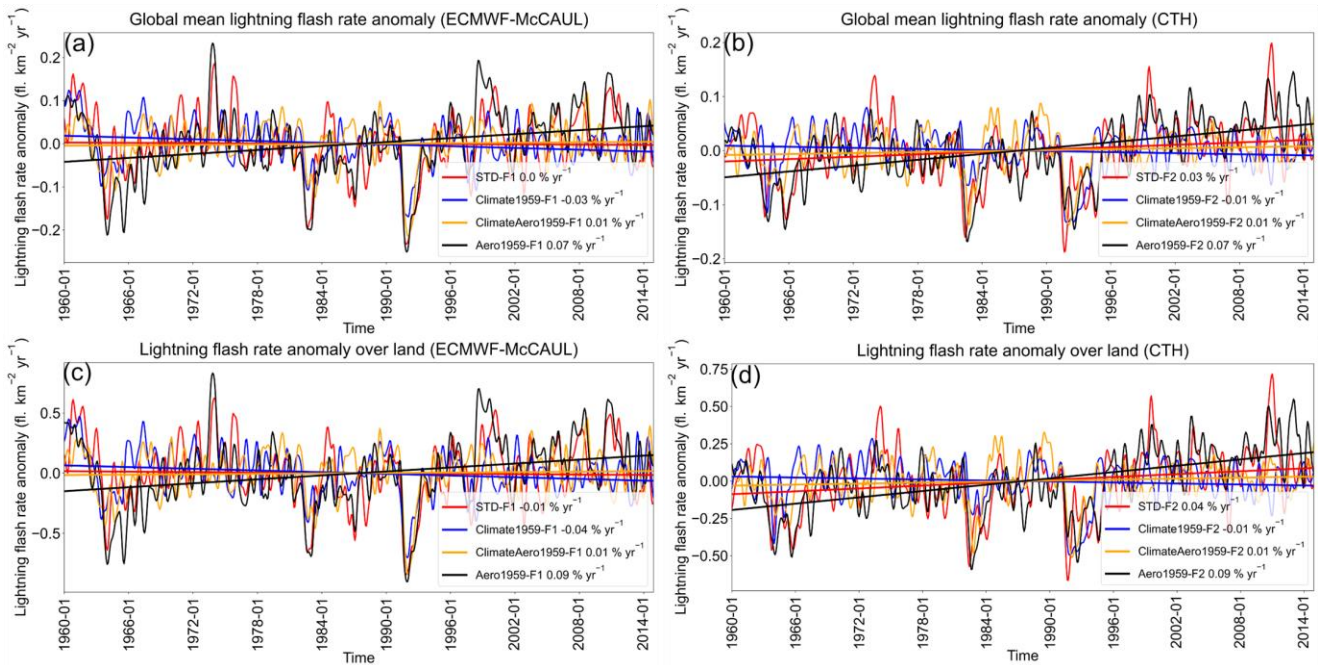
348 **3.2 Effects of global warming and increases in AeroPEs on historical lightning–LNO_x trends**

349 As introduced in Sect. 1, global warming and changes in AeroPEs are the two main factors which influence long-term (1960–
350 2014) historical lightning trends (Hereinafter, historical lightning trends represent lightning trends of 1960–2014.). Evidence
351 shows that the Pacific Decadal Oscillation (PDO) can also affect lightning trends over decadal time scales (Macias Fauria and
352 Johnson, 2006; Mallick et al., 2022), and further research is anticipated to verify it. To analyze the effects of global warming
353 on historical lightning trends, we designed and conducted two sets of experiments: one set of experiments including “global
354 warming” (STD-F1/F2) and another set of experiments excluding “global warming” (Climate1959-F1/F2). Figures 4a and 4b
355 respectively depict the global surface temperature anomalies calculated using the ECMWF-McCAUL and CTH schemes. The
356 STD and Aero1959 experiments show an increasing trend (around 0.11 K decade⁻¹) of global mean surface temperature
357 anomalies, which closely approximates the trend (around 0.15 K decade⁻¹) obtained from NOAA’s National Centers for
358 Environmental Information (NCEI) (Figs. 4c, 4f). Global temperature change data from 1880 to the present are available from
359 the NCEI, which tracks variations of the Earth’s temperature based on thousands of stations’ observation data around the globe
360 (Climate at a Glance | National Centers for Environmental Information (NCEI), 2022). When the prescribed SSTs/sea ice fields
361 and GHGs concentrations were fixed to 1959 throughout the simulation period, the simulated trends of global mean surface
362 temperature anomalies turned out to be flat (Climate1959 and ClimateAero1959). To elucidate the effects of increases in
363 AeroPEs on averaged surface temperature to the greatest extent possible, we also show the averaged surface temperature
364 anomaly only over land regions (Figs. 4d–4f). The simulated global mean land surface temperature anomalies are also well-
365 matched with the NCEI observational data. The aerosol cooling effect can be more evident when only examining surface
366 temperature trends averaged over land (Figs. 4d–4e).



367

368 **Figure 4: Monthly time-series data of global mean surface temperature anomalies with 1-D Gaussian (Denosing) filter applied and**
 369 **their fitting curves calculated from the outputs of numerical experiments (a–b) and obtained from NCEI (c). Panels (d)–(f) are the**
 370 **same as panels (a)–(c), but the averaged surface temperature anomalies are only calculated within the global land regions. The trends**
 371 **of the fitting curves in K decade⁻¹ are also presented in the legends.**



372

373 **Figure 5: Panels (a) and (b) show monthly time-series data of global mean LFR anomalies with 1-D Gaussian (Denosing) Filter**
 374 **applied and their fitting curves of different experiments simulated respectively using the ECMWF-McCAUL scheme and CTH**
 375 **scheme. Panels (c) and (d) are the same as panels (a) and (b), except that the averaged LFR anomalies are calculated only within**
 376 **global land regions. Trends of the fitting curves ($\% \text{ yr}^{-1}$) are also shown in the legends.**

377

378 **Table 3: A statistical summary of the trends shown in Fig. 5 by Mann–Kendall rank statistic and Sen’s slope estimator. The monthly**
 379 **time-series data of global or land mean LFR anomalies were estimated by Mann–Kendall rank statistic and Sen’s slope estimator.**
 380 **The column “Trend” shows whether these are significant trends with the significance set as 5%, as well as the percentage trends in $\%$**
 381 **yr^{-1} estimated by linear regression. The “ p -value” is calculated during Mann-Kendall trend test. “Slope” shows Sen’s slope of trend.**
 382 **Q_{\min} and Q_{\max} respectively denote the lower and upper limits of the 95% confidence interval of Sen’s slope.**

Experiment	Trend	p -value	Slope	Q_{\min}	Q_{\max}
<u>STD-F1 (global)</u>	<u>No trend, 0.0 % yr^{-1}</u>	<u>$p > 0.05$</u>	<u>0.0</u>	<u>-0.0001</u>	<u>0.0</u>
<u>Climate1959-F1 (global)</u>	<u>Decreasing, -0.03 % yr^{-1}</u>	<u>$p < 0.01$</u>	<u>-0.0001</u>	<u>-0.0001</u>	<u>0.0</u>
<u>ClimateAero1959-F1 (global)</u>	<u>No trend, 0.01 % yr^{-1}</u>	<u>$p > 0.05$</u>	<u>0.0</u>	<u>0.0</u>	<u>0.0001</u>
<u>Aero1959-F1 (global)</u>	<u>Increasing, 0.07 % yr^{-1}</u>	<u>$p < 0.01$</u>	<u>0.0001</u>	<u>0.0001</u>	<u>0.0002</u>
<u>STD-F1 – Climate1959-F1 (global)</u>	<u>No trend, 0.03 % yr^{-1}</u>	<u>$p > 0.05$</u>	<u>0.0001</u>	<u>0.0</u>	<u>0.0001</u>
<u>STD-F1 – Aero1959-F1 (global)</u>	<u>Decreasing, -0.07 % yr^{-1}</u>	<u>$p < 0.01$</u>	<u>-0.0001</u>	<u>-0.0002</u>	<u>-0.0001</u>
<u>STD-F1 (land)</u>	<u>No trend, -0.01 % yr^{-1}</u>	<u>$p > 0.05$</u>	<u>0.0</u>	<u>-0.0002</u>	<u>0.0001</u>
<u>Climate1959-F1 (land)</u>	<u>Decreasing, -0.04 % yr^{-1}</u>	<u>$p < 0.01$</u>	<u>-0.0002</u>	<u>-0.0004</u>	<u>-0.0001</u>
<u>ClimateAero1959-F1 (land)</u>	<u>No trend, 0.01 % yr^{-1}</u>	<u>$p > 0.05$</u>	<u>0.0001</u>	<u>-0.0001</u>	<u>0.0002</u>

<u>Aero1959-F1 (land)</u>	<u>Increasing, 0.09 % yr⁻¹</u>	<u>$p < 0.01$</u>	<u>0.0005</u>	<u>0.0003</u>	<u>0.0006</u>
<u>STD-F1 – Climate1959-F1 (land)</u>	<u>No trend, 0.03 % yr⁻¹</u>	<u>$p > 0.05$</u>	<u>0.0002</u>	<u>-0.0001</u>	<u>0.0004</u>
<u>STD-F1 – Aero1959-F1 (land)</u>	<u>Decreasing, -0.10 % yr⁻¹</u>	<u>$p < 0.01$</u>	<u>-0.0005</u>	<u>-0.0007</u>	<u>-0.0003</u>
<u>STD-F2 (global)</u>	<u>Increasing, 0.03 % yr⁻¹</u>	<u>$p < 0.01$</u>	<u>0.0001</u>	<u>0.0</u>	<u>0.0001</u>
<u>Climate1959-F2 (global)</u>	<u>No trend, -0.01 % yr⁻¹</u>	<u>$p > 0.05$</u>	<u>0.0</u>	<u>-0.0001</u>	<u>0.0</u>
<u>ClimateAero1959-F2 (global)</u>	<u>No trend, 0.01 % yr⁻¹</u>	<u>$p > 0.05$</u>	<u>0.0</u>	<u>0.0</u>	<u>0.0001</u>
<u>Aero1959-F2 (global)</u>	<u>Increasing, 0.07 % yr⁻¹</u>	<u>$p < 0.01$</u>	<u>0.0001</u>	<u>0.0001</u>	<u>0.0002</u>
<u>STD-F2 – Climate1959-F2 (global)</u>	<u>Increasing, 0.04 % yr⁻¹</u>	<u>$p < 0.01$</u>	<u>0.0001</u>	<u>0.0</u>	<u>0.0001</u>
<u>STD-F2 – Aero1959-F2 (global)</u>	<u>Decreasing, -0.04 % yr⁻¹</u>	<u>$p < 0.01$</u>	<u>-0.0001</u>	<u>-0.0001</u>	<u>0.0</u>
<u>STD-F2 (land)</u>	<u>Increasing, 0.04 % yr⁻¹</u>	<u>$p < 0.01$</u>	<u>0.0003</u>	<u>0.0001</u>	<u>0.0004</u>
<u>Climate1959-F2 (land)</u>	<u>No trend, -0.01 % yr⁻¹</u>	<u>$p > 0.05$</u>	<u>-0.0001</u>	<u>-0.0002</u>	<u>0.0</u>
<u>ClimateAero1959-F2 (land)</u>	<u>No trend, 0.01 % yr⁻¹</u>	<u>$p > 0.05$</u>	<u>0.0001</u>	<u>0.0</u>	<u>0.0002</u>
<u>Aero1959-F2 (land)</u>	<u>Increasing, 0.09 % yr⁻¹</u>	<u>$p < 0.01$</u>	<u>0.0006</u>	<u>0.0004</u>	<u>0.0007</u>
<u>STD-F2 – Climate1959-F2 (land)</u>	<u>Increasing, 0.05 % yr⁻¹</u>	<u>$p < 0.01$</u>	<u>0.0003</u>	<u>0.0001</u>	<u>0.0005</u>
<u>STD-F2 – Aero1959-F2 (land)</u>	<u>Decreasing, -0.05 % yr⁻¹</u>	<u>$p < 0.01$</u>	<u>-0.0003</u>	<u>-0.0005</u>	<u>-0.0001</u>

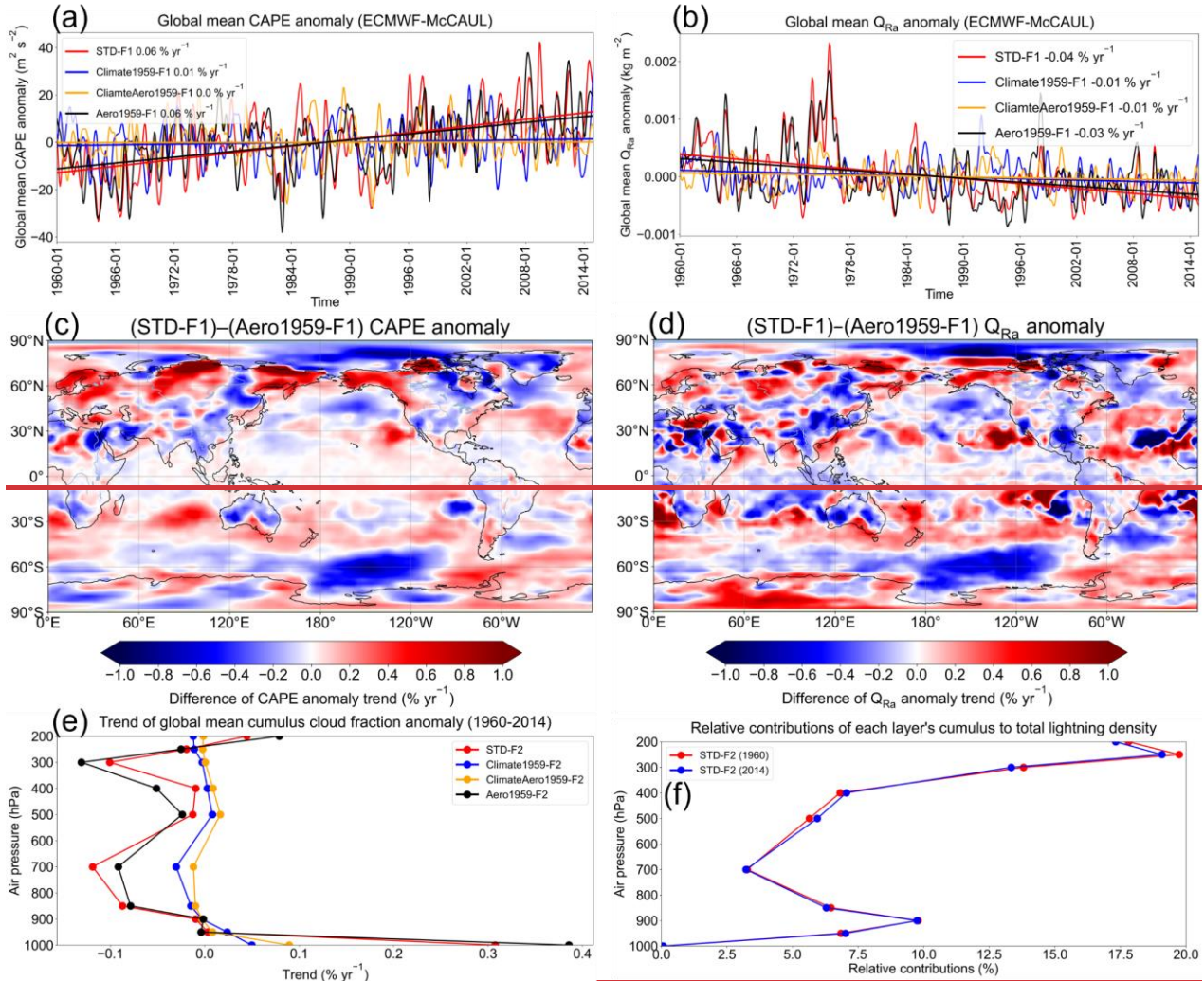
383

384 Figure 5, panels (a) and (b) respectively portray the global mean LFR anomalies and their fitting curves obtained from the
385 outputs of the ECMWF-McCAUL scheme and CTH scheme. Besides, we displayed in Table 3 the statistical summary of the
386 trends in Fig. 5 utilizing Mann–Kendall rank statistic and Sen’s slope estimator. The global lightning trend obtained from the
387 STD-F1 experiment turned out to be statistically flat (0.0% yr⁻¹), whereas the outputs of the STD-F2 experiment exhibit a ~~not~~
388 significant increasing global lightning trend (0.03% yr⁻¹) determined using the Mann–Kendall rank statistic (significance
389 inferred for 5%).

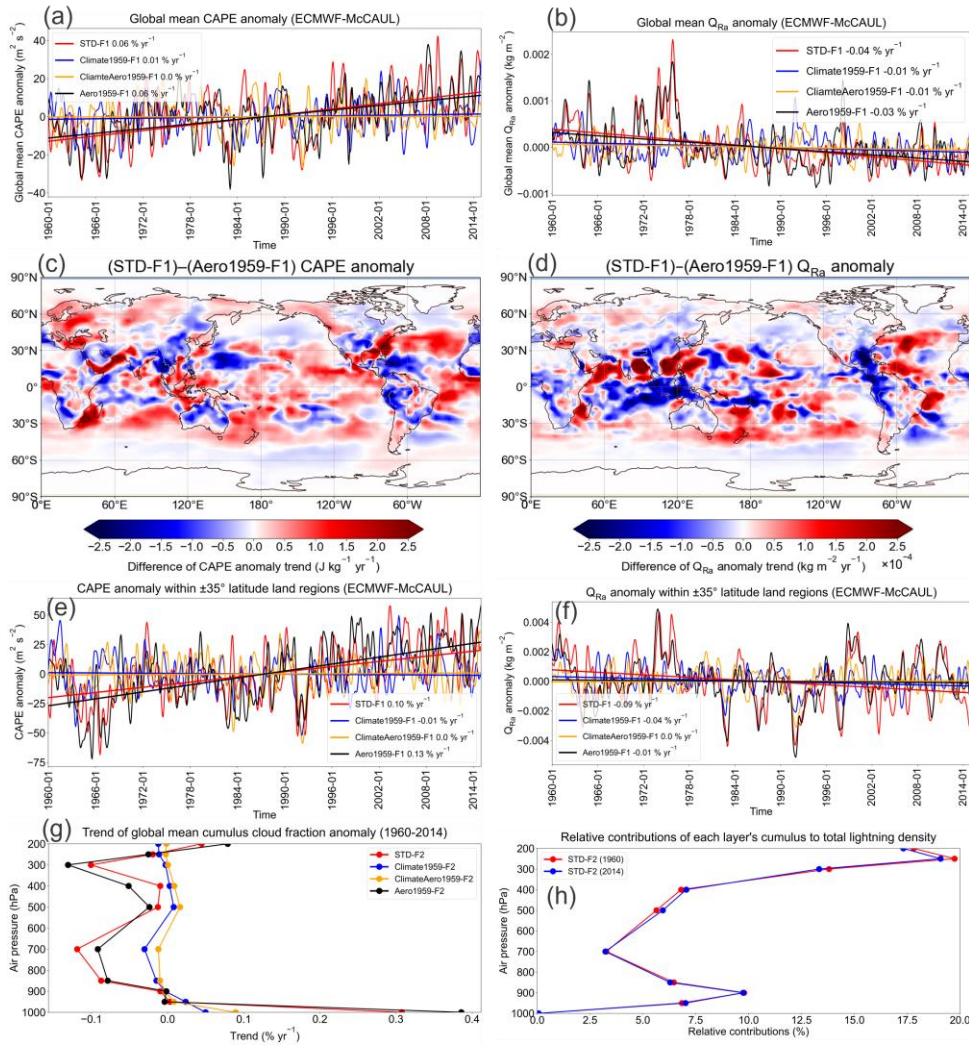
390

391 Comparison of the lightning trends calculated from the STD and Climate1959 experiments showed that both lightning schemes
392 demonstrated that historical global warming (1960–2014) enhances the global lightning trends toward positive trends (around
393 0.03% yr⁻¹ or 3% K⁻¹). Global warming effects on historical lightning trends were evaluated as significant using the Mann–
394 Kendall rank statistic, with significance inferred for 5%, when using the CTH scheme, but not in the case of the ECMWF-
395 McCAUL scheme. ~~The~~ (see rows “STD-F1 – Climate1959-F1 (global)” and “STD-F2 – Climate1959-F2 (global)
396 ” in Table 3). As shown in Table 3, the differences in global lightning trends simulated by the STD-F1/F2 and Aero1959-
397 F1/F2 experiments indicate that the increases in AeroPEs during 1960–2014 significantly suppress the global lightning trends
398 (-0.07% yr⁻¹ – -0.04% yr⁻¹). It is noteworthy that this suppression of lightning trends is only attributable to aerosol radiative
399 effects. Further research must be conducted to elucidate the long-term effects of aerosols on lightning through aerosol
400 microphysical effects. We also investigated lightning trends only over land regions (Figs. 5c–5d and Table 3) to ascertain the
401 effects of changes in AeroPEs to the greatest extent possible. When observing the lightning trends over land only, the degree

402 of suppression of lightning trends attributable to increases in AeroPEs expands to $-0.10\% \text{ yr}^{-1} - -0.05\% \text{ yr}^{-1}$, which is
 403 attributable to most AeroPEs and their growth coming from land regions. It is noteworthy that we used the same SSTs/sea ice
 404 data in the Aero1959 as those used for STD experiments. The SSTs/sea ice data also reflected the effects of increases in
 405 AeroPEs. Therefore, we might underestimate the effects of increases in AeroPEs on lightning trends by comparing the results
 406 of STD and Aero1959 experiments.



407



408

409 **Figure 6:** Panels (a) and (b) respectively show monthly time-series data of global mean CAPE and Q_{Ra} anomalies with 1-D Gaussian
 410 (Denosing) filter applied and their fitting curves simulated using the ECMWF-McCAUL scheme. Panels (c) and (d) respectively
 411 show differences in the CAPE anomaly trend ($\text{J kg}^{-1} \text{yr}^{-1}$) and Q_{Ra} anomaly trend ($\text{kg m}^{-2} \text{yr}^{-1}$) of the STD-F1 and Aero1959-
 412 F1 experiments in the global map. **Panels (e) and (f) respectively show monthly time-series data of $\pm 35^\circ$ latitude land region mean**
 413 **CAPE and Q_{Ra} anomalies with 1-D Gaussian (Denosing) filter applied and their fitting curves simulated using the ECMWF-**
 414 **McCAUL scheme.** Figure 6(g) portrays the vertical profiles of the trend of global mean cumulus cloud fraction anomaly simulated
 415 by the CTH scheme. Panel (h) depicts the relative contributions of each layer's cumulus to total lightning density in 1960 and 2014,
 416 as calculated from the outputs of the STD-F2 experiment.

417

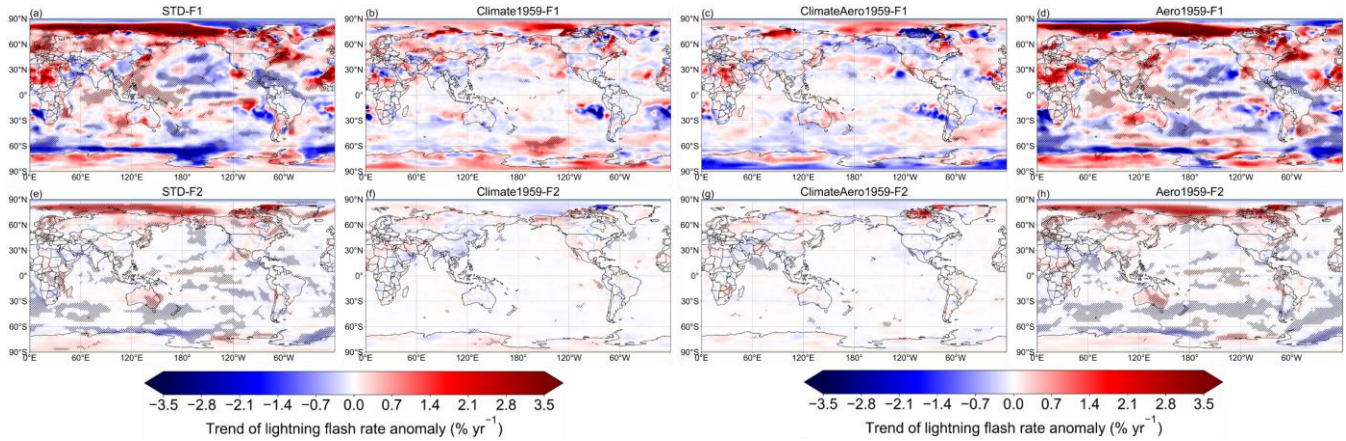
418 For the ECMWF-McCAUL scheme, model outputs affirm that global warming can enhance the global mean CAPE anomaly
 419 slightly and suppress the global mean Q_{Ra} anomaly (Figs. 6a–6b). Earlier studies have also indicated that the total solid (cloud

420 ice, snow, and graupel) mass mixing ratio within charge separation regions is lower under global warming. Moreover, possible
421 explanations are given in those studies (Finney et al., 2018; Romps, 2019). Because global warming enhances global
422 convection activities, and because lightning formation is highly related to convection activity, global warming enhances the
423 historical global lightning trend simulated using the ECMWF-McCAUL scheme, mainly as a result of the simulated CAPE
424 trend, which is enhanced by global warming.

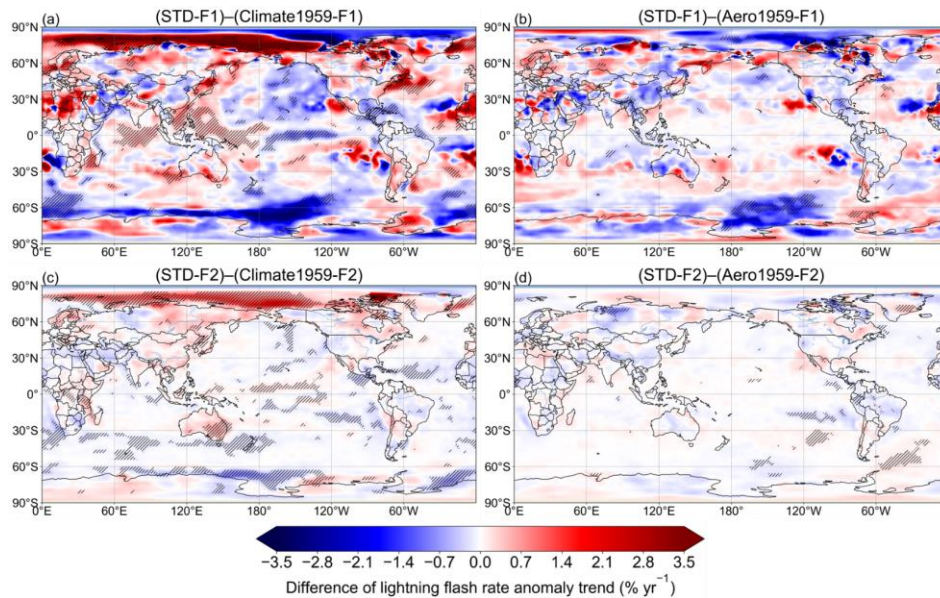
425
426 The past increases in AeroPEs exert negligible effects on the trends of global mean CAPE and Q_{Ra} anomalies, as displayed in
427 Figs. 6a–6b. ~~However, the past increases in AeroPEs suppress the CAPE and Q_{Ra} trend within the tropical and subtropical~~
428 ~~terrestrial regions, where lightning densities are high (Figs. 6e–6d). However, as also demonstrated in our study (see Fig. 1),~~
429 ~~most lightning flashes occur over tropical and subtropical land regions. It is displayed in Figs. 6c–6d that the past increases in~~
430 ~~AeroPEs mostly suppress the CAPE and Q_{Ra} absolute trends within regions with high lightning densities. We further~~
431 ~~investigated the trends of $\pm 35^\circ$ latitude land region mean CAPE and Q_{Ra} anomalies, and the results are portrayed in Figs.~~
432 ~~6e–6f. Figs. 6e–6f show that past increases in AeroPEs significantly suppress the Q_{Ra} trend ($-0.08\% \text{ yr}^{-1}$) and slightly suppress~~
433 ~~the CAPE trend ($-0.03\% \text{ yr}^{-1}$) within $\pm 35^\circ$ latitude land regions.~~ Weaker convection activities (smaller CAPE) and fewer
434 hydrometeors (cloud ice, graupel, snow) in the charge separation regions ($0^\circ\text{C} - -25^\circ\text{C}$ isotherm) engender less lightning.
435 ~~These are~~In the case of the ECMWF-McCAUL scheme, CAPE and Q_{Ra} trends were suppressed within $\pm 35^\circ$ latitude terrestrial
436 ~~regions. This constitutes~~ the main ~~causes~~reason for the suppression of the historical global lightning trends induced by increases
437 in AeroPEs through aerosol radiative effects. It is noteworthy that, because the aerosol microphysical effects are only
438 considered in the grid-scale large-scale condensation scheme, our study might underestimate the aerosol microphysical effects
439 which can enhance the trends of Q_{Ra} and LFR toward the positive direction.

440
441 To explain the results simulated by the CTH scheme, we investigated the vertical profiles of the trend of the global mean
442 cumulus cloud fraction anomaly (Fig. 6e6g). Investigating cumulus cloud fraction is reasonable because each model layer's
443 cumulus cloud fractions are used to weight the calculated lightning densities from that layer in the CTH scheme, as introduced
444 in equations (3) and (4). Figure 6f6h shows the relative contributions of each model layer's cumulus to the calculated global
445 total lightning densities in 1960 and 2014 obtained using the CTH scheme. As Fig. 6f6h displayed, the vertical profiles of
446 relative contribution in 1960 and 2014 are almost identical. Cumulus convection is positively correlated with lightning
447 formation, which is the scientific basis of parameterizing lightning densities using the cumulus cloud top height: the CTH
448 scheme. Historical global warming enhances the lightning trend simulated by the CTH scheme mainly because the simulated
449 historical global warming increases the cumulus reaching 200 hPa, which contributes greatly to the simulated global total
450 lightning density (Figs. 6e–6f6g–6h). The increases in the deep convective cloud are regarded as related to the increases in
451 tropopause height attributable to global warming, as shown in Fig. S2. The past increases in AeroPEs suppress the lightning
452 trend simulated by the CTH scheme because increases in AeroPEs decrease the cumulus reaching 200 hPa as well as the

453 cumulus within the lower to middle troposphere by aerosol radiative effects (Fig. 6e6g). In addition, in the supplement, we
 454 present a figure (Fig. S3) resembling Fig. 6, but which includes only consideration of land regions. The mechanisms of global
 455 warming and increases in AeroPEs affecting lightning trends over land regions are similar to those described above on a global
 456 scale. We do not discuss details of them here.



458
 459 **Figure 7: Trends of LFR anomaly ($\% \text{ yr}^{-1}$) during 1960–2014 on the two-dimensional map. The trend at every point was calculated**
 460 **from the function of approximating curve for the 1960–2014 time-series data (LFR anomaly) at each grid cell. The area in which the**
 461 **trend was found to be significant by the Mann–Kendall rank statistic test (significance inferred for 5%) is marked with hatched**
 462 **lines.**
 463

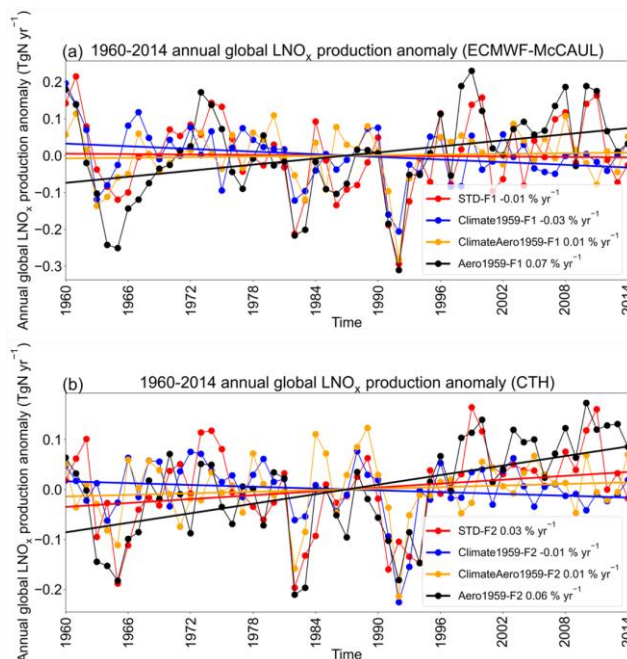


464

465 **Figure 8: Differences in trends of LFR anomaly during 1960–2014 on the global map. The area in which the trend of the differences**
466 **of LFR anomaly time-series data was found to be significant by the Mann–Kendall rank statistic test (significance inferred for 5%)**
467 **is marked with hatched lines.**

468

469 We also investigated lightning trends simulated in different experiments with the global map (Fig. 7). Both the ECMWF-
470 McCAUL and the CTH schemes show that lightning increased significantly in most parts of the Arctic region and decreased
471 in some parts of the Southern Ocean during 1960–2014 (Figs. 7a, 7e). The significant lightning trends presented in Figs. 7a
472 became nearly nonexistent when the climate simulations were fixed to 1959 (Figs. 7b, 7f), indicating the considerable effects
473 of global warming on the trend of global lightning activities. Furthermore, the effects of past global warming and increases in
474 AeroPEs on the lightning trends on the global map are displayed in Fig. 8. Figures 8a and 8c show that past global warming
475 enhances lightning activities within the Arctic region and Japan, which is consistent with findings of an earlier study from
476 which Japan thunder day data were reported (Fujibe, 2017). Figures 8a and 8c also show that historical global warming
477 suppresses lightning activities around New Zealand and some parts of the Southern Ocean. Both lightning schemes
478 demonstrated that the historical increases in AeroPEs suppress lightning activities in some parts of the Southern Ocean and
479 South America. The ECMWF-McCAUL scheme also suggests that historical increases in AeroPEs suppress lightning activities
480 by aerosol radiative effects in some parts of India and China, where AeroPEs increased dramatically during 1960–2014 because
481 of rapid economic development and energy consumption. Many observation-based studies indicate that aerosols can invigorate
482 lightning activities in some regions of China and India, typically under relatively clean conditions (e.g., $AOD < 1.0$), which is
483 attributable to the aerosol microphysical effects (Wang et al., 2011; Zhao et al., 2017; Lal et al., 2018; Liu et al., 2020; Shi et
484 al., 2020; Zhao et al., 2020). Therefore, a total positive effect of aerosol on historical lightning trends in China and India cannot
485 be ruled out. We further provided the same figures as Figs. 7 and 8, but using different units ($\text{fl. km}^{-2} \text{ yr}^{-2}$) in the supplementary
486 information (Figs. S4 and S5). Figures S4 and S5 show that the absolute lightning trends ($\text{fl. km}^{-2} \text{ yr}^{-2}$) and the effects of global
487 warming and increases in AeroPEs on the absolute lightning trends are slight in high-latitude regions but prominent in tropical
488 areas.



489
 490 **Figure 9: Time-series data of 1960–2014 annual global LNO_x production anomalies (TgN yr⁻¹) and their fitting curves simulated**
 491 **using the ECMWF-McCAUL scheme (a) and the CTH scheme (b). Trends of the fitting curves in percent per year are presented in**
 492 **the legends.**

493
 494 **Table 4: A statistical summary of the trends shown in Fig. 9 by Mann–Kendall rank statistic and Sen’s slope estimator. The time-**
 495 **series data of annual global LNO_x production anomalies were estimated by Mann–Kendall rank statistic and Sen’s slope estimator.**
 496 **The column “Trend” shows whether these are significant trends with the significance set as 5%, as well as the percentage trends in %**
 497 **yr⁻¹ estimated by linear regression. The “p-value” is calculated during Mann-Kendall trend test. “Slope” shows Sen’s slope of trend.**
 498 **Q_{min} and Q_{max} respectively denote the lower and upper limits of the 95% confidence interval of Sen’s slope.**

499

<u>Experiment</u>	<u>Trend</u>	<u>p-value</u>	<u>Slope</u>	<u>Q_{min}</u>	<u>Q_{max}</u>
<u>STD-F1</u>	<u>No trend, -0.01 % yr⁻¹</u>	<u>p > 0.05</u>	<u>-0.0001</u>	<u>-0.002</u>	<u>0.0018</u>
<u>Climate1959-F1</u>	<u>Decreasing, -0.03 % yr⁻¹</u>	<u>p < 0.05</u>	<u>-0.0011</u>	<u>-0.0024</u>	<u>-0.0001</u>
<u>ClimateAero1959-F1</u>	<u>No trend, 0.01 % yr⁻¹</u>	<u>p > 0.05</u>	<u>0.0003</u>	<u>-0.0008</u>	<u>0.0013</u>
<u>Aero1959-F1</u>	<u>Increasing, 0.07 % yr⁻¹</u>	<u>p < 0.01</u>	<u>0.003</u>	<u>0.0011</u>	<u>0.0048</u>
<u>STD-F1 – Climate1959-F1</u>	<u>No trend, 0.02 % yr⁻¹</u>	<u>p > 0.05</u>	<u>0.0009</u>	<u>-0.0009</u>	<u>0.0025</u>
<u>STD-F1 – Aero1959-F1</u>	<u>Decreasing, -0.08 % yr⁻¹</u>	<u>p < 0.01</u>	<u>-0.003</u>	<u>-0.004</u>	<u>-0.0021</u>
<u>STD-F2</u>	<u>Increasing, 0.03 % yr⁻¹</u>	<u>p < 0.05</u>	<u>0.0013</u>	<u>0.0001</u>	<u>0.0024</u>
<u>Climate1959-F2</u>	<u>No trend, -0.01 % yr⁻¹</u>	<u>p > 0.05</u>	<u>-0.0007</u>	<u>-0.0014</u>	<u>0.0001</u>
<u>ClimateAero1959-F2</u>	<u>No trend, 0.01 % yr⁻¹</u>	<u>p > 0.05</u>	<u>0.0005</u>	<u>-0.0004</u>	<u>0.0015</u>

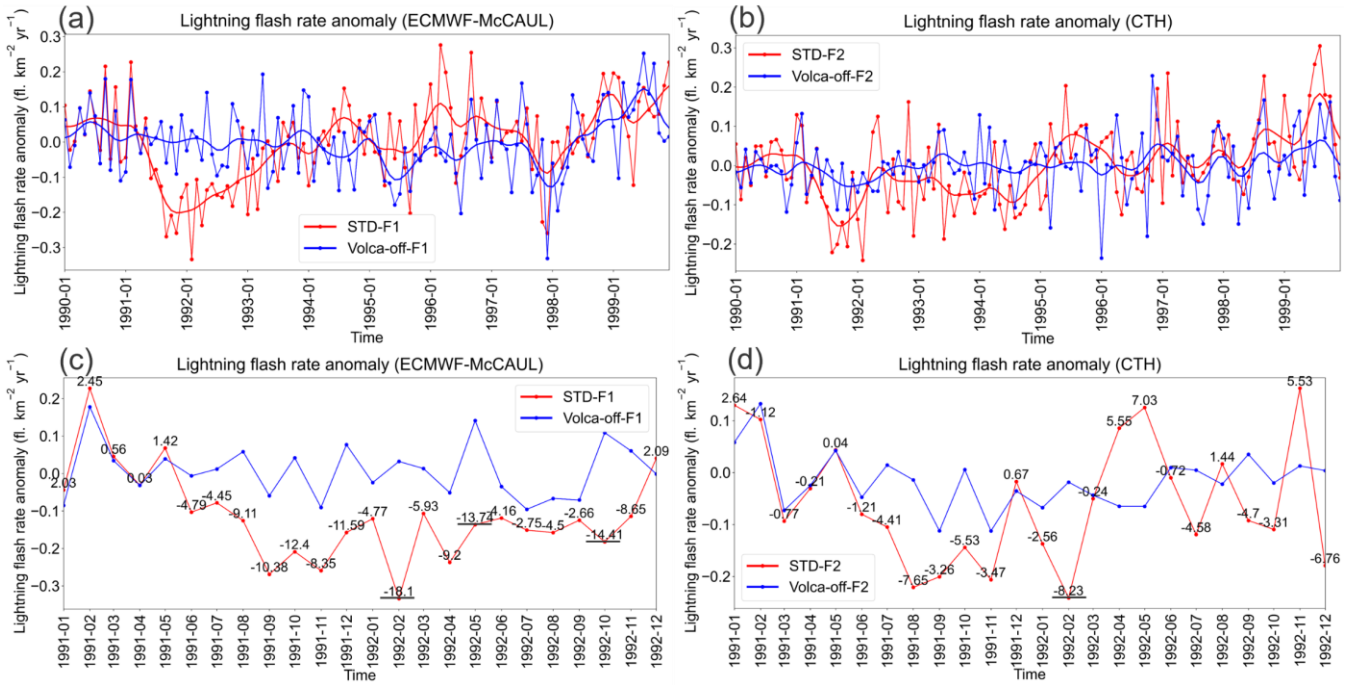
<u>Aero1959-F2</u>	<u>Increasing, 0.06 % yr⁻¹</u>	<u>p < 0.01</u>	<u>0.0033</u>	<u>0.0019</u>	<u>0.0046</u>
<u>STD-F2 – Climate1959-F2</u>	<u>Increasing, 0.04 % yr⁻¹</u>	<u>p < 0.01</u>	<u>0.0021</u>	<u>0.0006</u>	<u>0.0033</u>
<u>STD-F2 – Aero1959-F2</u>	<u>Decreasing, -0.03 % yr⁻¹</u>	<u>p < 0.01</u>	<u>-0.0019</u>	<u>-0.0029</u>	<u>-0.001</u>

500

501 Trends in historical annual global LNO_x emissions for different scenarios are generally consistent with trends in historical
502 global mean LFRs, as shown in Figs. 5a–5b and Fig. 9. This finding is not surprising because, as the lightning NO_x emission
503 parameterizations introduced in Sect. 2.2 show, the simulated LFRs are linearly related to the simulated LNO_x emissions in
504 our study. ~~The results presented in Fig. 9~~Comparison of the LNO_x trends calculated from the STD and Climate1959
505 experiments showed that both lightning schemes demonstrated that historical global warming (1960–2014) enhances the global
506 LNO_x trends toward positive trends (0.02% yr⁻¹–0.04% yr⁻¹). Global warming effects on historical LNO_x trends were evaluated
507 as significant using the Mann–Kendall rank statistic, with significance inferred for 5%, when using the CTH scheme, but not
508 in the case of the ECMWF-McCAUL scheme (see rows “STD-F1 – Climate1959-F1” and “STD-F2 – Climate1959-F2” in
509 Table 4). As shown in Table 4, the differences in global LNO_x trends simulated by the STD and Aero1959 experiments indicate
510 that the increases in AeroPEs during 1960–2014 significantly suppress the global LNO_x trends (-0.08% yr⁻¹– -0.03% yr⁻¹). The
511 results presented in Fig. 9 and Table 4 imply that historical global warming and increases in AeroPEs can affect atmospheric
512 chemistry and can engender feedback by influencing LNO_x emissions.

513 3.3 Pinatubo volcanic eruption effects on historical lightning–LNO_x trends

514 We estimate the Pinatubo eruption effects on historical lightning–LNO_x trends and variation by comparing the simulation
515 results of STD and Volca-off experiments. The simulated global mean LFRs by STD and Volca-off experiments are the same
516 until April 1991. They then begin to show differences from May 1991 (The time series of global mean LFRs is not shown.).
517 This result is reasonable because the Pinatubo volcanic perturbations are removed from SAC during June 1991 – May 1996 in
518 the Volca-off experiments by equation (11), and because the SAC of May 1991 used in CHASER is interpolated between the
519 SAC of April 1991 and June 1991.



520

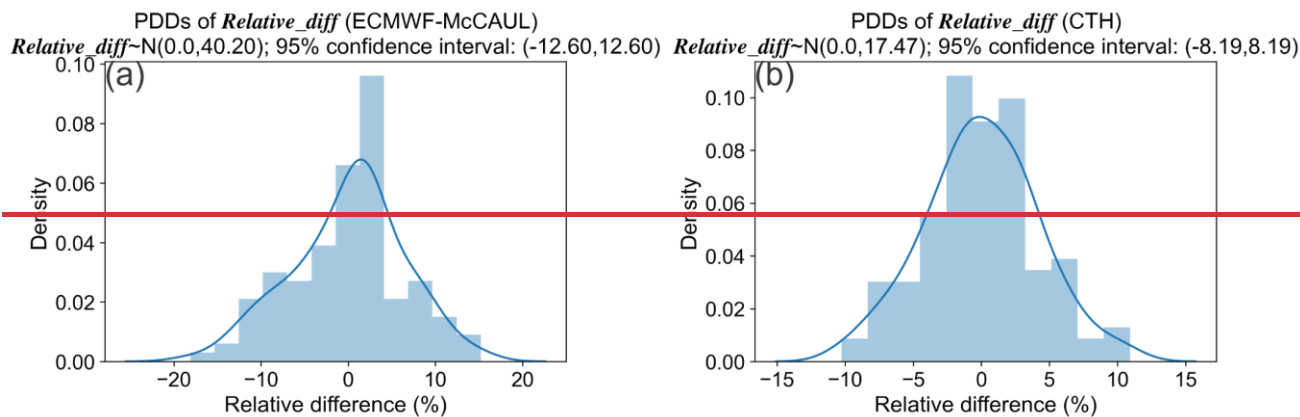
521 **Figure 10: Time series of LFR anomalies during 1990–1999 or during 1991–1992. Panels (a) and (b) show the time series of LFR**
 522 **anomalies and their smoothed curves by 1-D Gaussian (Denosing) filter for 1990–1999. Panels (c) and (d) present the time series of**
 523 **LFR anomalies during 1991–1992. Values shown over the red lines in panels (c) and (d) are *Relative_diff* calculated using equation**
 524 **12.**

525

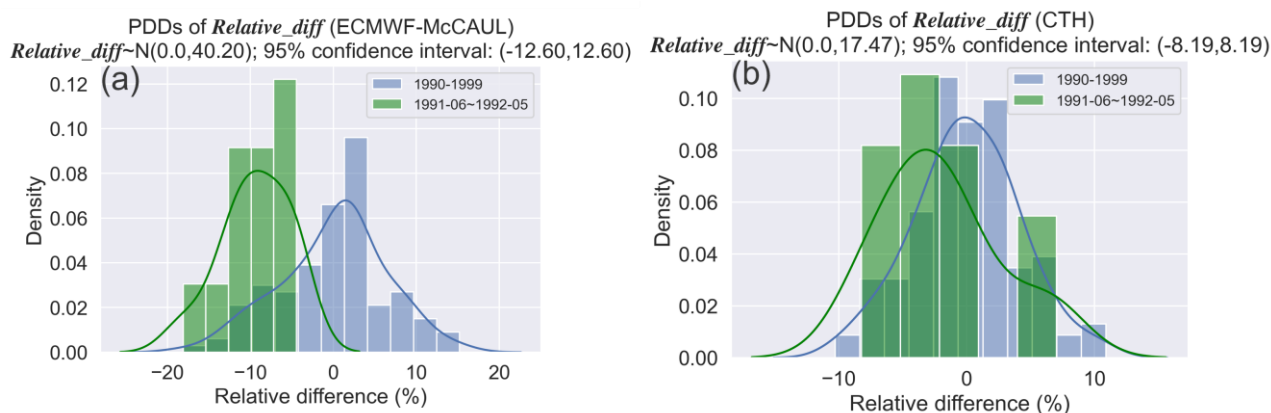
526 Figures 10c–10d portray the time series of LFR anomalies and *Relative_diff* (values over the red lines) during 1991–1992.
 527 *Relative_diff* are relative differences of the global mean LFR anomalies between STD and Volca-off experiments
 528 calculated using the following equation.

$$529 \text{ *Relative_diff* = } 100\% \times \frac{\text{LFR}_{STD} - \text{LFR}_{Volca-off}}{\text{LFR}_{Volca-off}} \quad (12)$$

530 In the equation, LFR_{STD} represents global mean LFR anomalies simulated by STD-F1/F2 experiments. $\text{LFR}_{Volca-off}$
 531 denotes global mean LFR anomalies simulated by Volca-off-F1/F2 experiments. $\text{LFR}_{Volca-off}$ symbolizes global mean LFRs
 532 simulated by Volca-off-F1/F2 experiments.



533

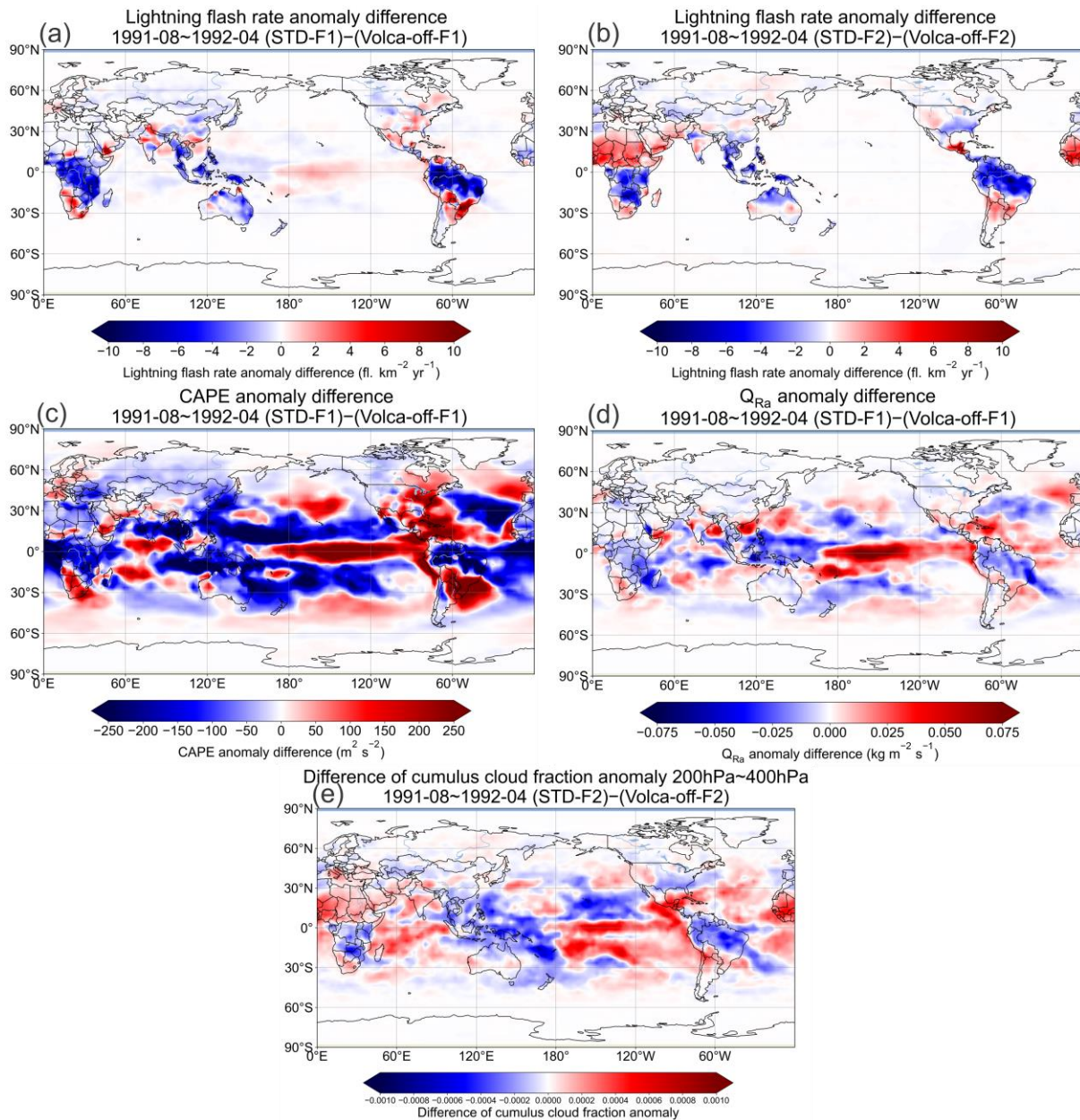


534

535 **Figure 11: Probability Density Distributions (PDDs) of *Relative_diff* obtained from monthly time-series data of *Relative_diff***
 536 **during 1990–1999. The 95% confidence interval of and 1991-06 – 1992-05 (a year after the Pinatubo eruption). The 1990–1999**
 537 ***Relative_diff* for both lighting schemes are normally distributed with $N(\mu, \sigma^2)$ displayed in the titles of this figure. The 95%**
 538 **confidence interval of 1990–1999 *Relative_diff* is also shown in the titles of this figure.**

539

540 The monthly time-series data of *Relative_diff* for 1990–1999 for both lightning schemes are calculated. The Probability
 541 Density Distributions (PDDs) of *Relative_diff* spanning 1990–1999 and 1991-06 – 1992-05 are displayed in Fig. 11. The
 542 1990–1999 *Relative_diff* presented in Fig. 11 (colored blue) are all normally distributed as determined by the Kolmogorov–
 543 Smirnov test. The 95% confidence interval of 1990–1999 *Relative_diff* is calculated and shown in the titles of Fig. 11. As
 544 displayed in Figs. 10c–10d, the underlined values (*Relative_diff*) exceeded the 95% confidence interval, indicating
 545 significant differences in the calculated global mean LFR anomalies by STD and Volca-off experiments. In other words, global
 546 lightning activities were suppressed significantly by the Pinatubo eruption during the first year after the eruption. The PDDs
 547 of 1991-06 – 1992-05 *Relative_diff* (colored green in Fig. 11) shifted to the left compared to the 1990–1999 PDDs,
 548 indicating that global lightning activities were suppressed in the first year after the eruption.



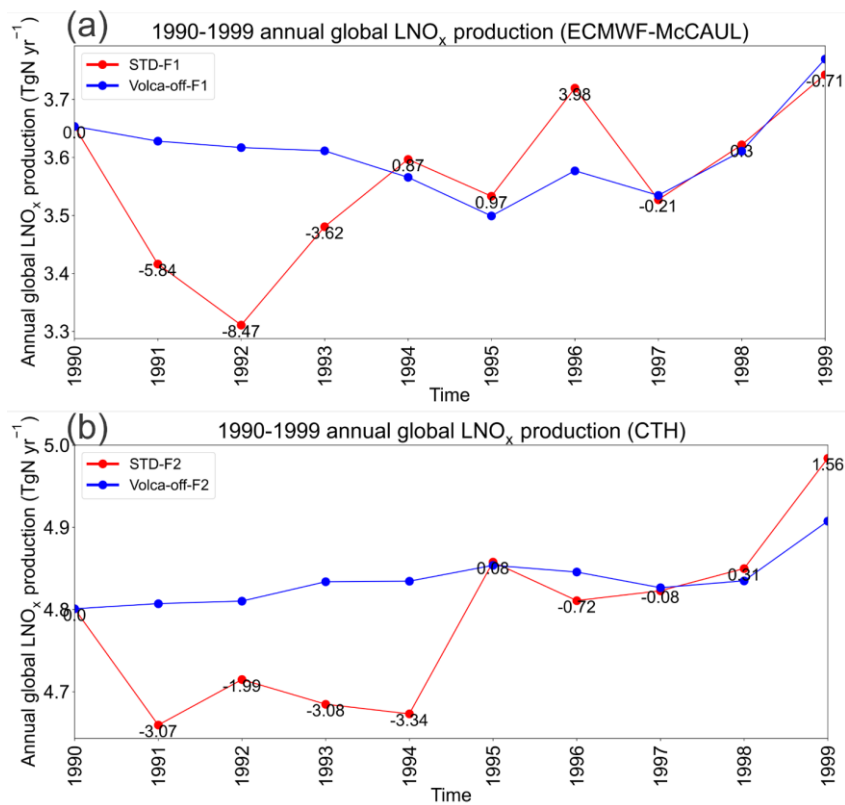
549

550 **Figure 12: 1991-08 – 1992-04 averaged LFR anomaly differences (a–b), CAPE anomaly differences (c), Q_{Ra} anomaly differences (d),**
 551 **and differences of 200 hPa – 400 hPa averaged cumulus cloud fraction anomaly between STD-F2 and Volca-off-F2 experiments (e)**
 552 **on the global map.**

553

554 Figures 12a–12b show 1991-08 – 1992-04 averaged LFR anomaly differences between STD and Volca-off experiments on
 555 the global map. We found from Figs. 12a–12b that lightning activities are suppressed significantly within the three hotspots of
 556 lightning activities (Central Africa, Maritime Continent, and South America) during 1991-08 – 1992-04, when the global mean

557 LFRs are found to be suppressed. To elucidate the potential reasons for the suppressed global lightning activities during the
 558 first year after the Pinatubo eruption, we first investigated the 1991-08 – 1992-04 averaged differences in CAPE and Q_{Ra}
 559 anomaly between STD-F1 and Volca-off-F1 (Figs. 12c–12d) because lightning densities are computed with CAPE and Q_{Ra}
 560 by the ECMWF-McCAUL scheme. Results showed that the Pinatubo eruption can engender apparent reductions of CAPE and
 561 Q_{Ra} within tropical and subtropical terrestrial regions (typically three hotspots of lightning activities) where lightning
 562 occurrence is frequent. These reductions constitute the main reason for the suppressed global lightning activities during the
 563 first year after the Pinatubo eruption simulated by the ECMWF-McCAUL scheme. We also examined the 1991-08 – 1992-04
 564 averaged differences of 200 hPa – 400 hPa averaged cumulus cloud fraction anomaly between STD-F2 and Volca-off-F2 on
 565 the global map (Fig. 12e). The cumulus cloud fractions of each model layer are used to weight the calculated lightning densities
 566 from that layer by the CTH scheme, as explained in Sect. 2.2. As depicted in Fig. 12e and Fig. S6, the Pinatubo eruption led
 567 to marked reductions in the middle to upper tropospheric cumulus cloud fractions during 1991-08 – 1992-04 over three hotspots
 568 of lightning activities (Central Africa, Maritime Continent, and South America). As displayed in Fig. 6f6h, the cumulus that
 569 reached the middle to upper troposphere is related closely to lightning formation. Consequently, the simulated global lightning
 570 activities by the CTH scheme were also suppressed considerably during the first year after the Pinatubo eruption.



571

572 **Figure 13: 1990–1999 annual global LNO_x emissions calculated from the STD and Volca-off experiments’ outputs simulated using**
573 **the ECMWF-McCAUL scheme (a) and the CTH scheme (b). Values over the red lines represent the relative differences (%) between**
574 **the red lines and blue lines, calculated with respect to the blue lines.**

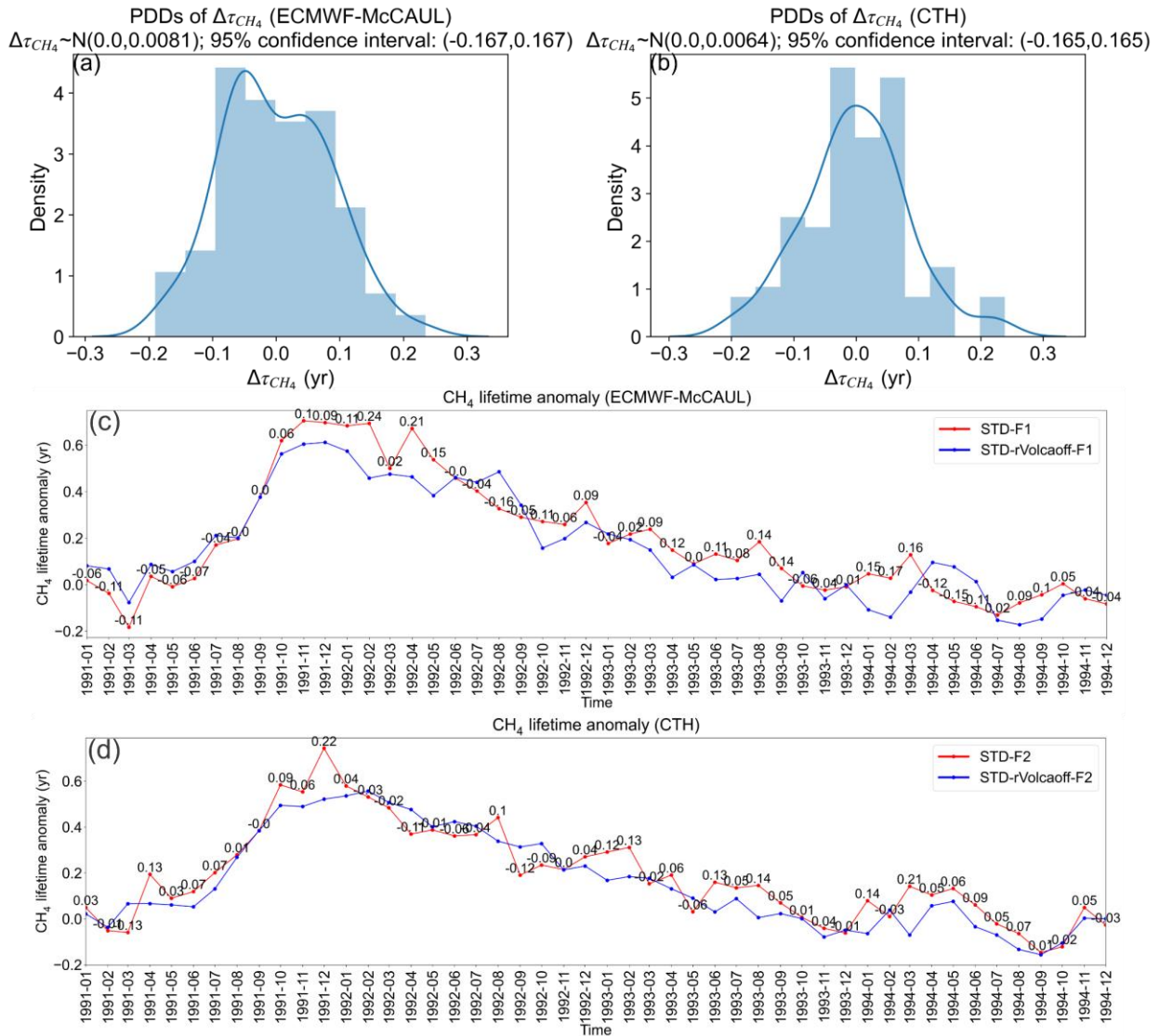
575

576 Aside from the global lightning activity suppression described earlier, the production of LNO_x might also decrease after the
577 Pinatubo eruption. To explore this conjecture, we compared the LNO_x emissions in STD and Volca-off experiments (Fig. 13).
578 In the case of the ECMWF-McCAUL scheme, the reduction of LNO_x emissions caused by the Pinatubo eruption started in
579 1991 (5.84%) and continued until 1993, with the highest percentage reduction occurring in 1992 (8.47%) (Fig. 13a). However,
580 the CTH scheme showed a slightly different scenario of LNO_x emissions reduction after the Pinatubo eruption. The LNO_x
581 emissions are almost evenly reduced during 1991–1994 in the case of the CTH scheme (Fig. 13b). In conclusion, our study
582 indicates that the Pinatubo eruption can engender reductions in global LNO_x emissions, which last 2–3 years. However, there
583 exists some uncertainty in evaluating the magnitude of the reductions: from 1.99% to 8.47% for the annual percentage
584 reduction found from our study.

585

586 The simulated reduced global LNO_x emissions caused by the Pinatubo eruption might influence atmospheric chemistry
587 significantly. Most importantly, the reduced global LNO_x emissions might reduce OH radical production and extend the global
588 mean tropospheric lifetime of methane against tropospheric OH radical, abbreviated hereinafter as the methane lifetime. We
589 investigated this point further by comparing the methane lifetime anomaly simulated by STD and STD-rVolcaoff experiments.
590 As introduced in Sect. 2.5, the settings of STD-rVolcaoff experiments are the same as those use for STD experiments, except
591 that they use the daily LNO_x emission rates calculated from the Volca-off experiments. We calculated the monthly CH₄ lifetime
592 anomalies during 1990–1999 and $\Delta\tau_{CH_4}$ (the difference of CH₄ lifetime anomaly between STD and STD-rVolcaoff
593 experiments), which are shown in Figs. 14c–14d. Figures 14a–14b display the PDDs of $\Delta\tau_{CH_4}$ monthly time series during
594 1990–1999. The $\Delta\tau_{CH_4}$ shown in Figs. 14a–14b are all normally distributed, as determined using the Kolmogorov–Smirnov
595 test. The 95% confidence interval of $\Delta\tau_{CH_4}$ is calculated and shown in the titles of Figs. 14a–14b. The annual global LNO_x
596 production averaged during 1990–1999 is 3.56 TgN yr⁻¹ for STD-F1 and 4.79 TgN yr⁻¹ for STD-F2. At this level of annual
597 global LNO_x production, we found that within the first two years after the Pinatubo eruption, the $\Delta\tau_{CH_4}$ exceeded the 95%
598 confidence interval simulated by both lighting schemes (1992-02 and 1992-04 in the case of the ECMWF-McCAUL scheme;
599 1991-12 in the case of the CTH scheme). However, the widely cited range of annual global LNO_x production is 2–8 TgN yr⁻¹
600 (Schumann and Huntrieser, 2007). Presuming that $\Delta\tau_{CH_4}$ responds linearly to the LNO_x emission level, and that the annual
601 global LNO_x production is 8 TgN yr⁻¹, then the extension of the CH₄ lifetime because of the reduced LNO_x emissions can reach
602 around 0.54 years for the ECMWF-McCAUL scheme. As a comparison, ultraviolet shielding effects caused by stratospheric
603 aerosols after the Pinatubo eruption led to the maximum increase of the methane lifetime by about 0.6 years (Figs. 14c–14d).

604



605

606 **Figure 14:** Panels (a) and (b) show the Probability Density Distributions (PDDs) of $\Delta\tau_{CH_4}$ obtained from the monthly time series
 607 data of $\Delta\tau_{CH_4}$ during 1990–1999. $\Delta\tau_{CH_4}$ represents the difference in CH_4 lifetime anomaly between STD and STD-rVolcaoff
 608 experiments. The 95% confidence interval of $\Delta\tau_{CH_4}$ is also presented in the titles of panels (a)–(b). Panels (c) and (d) show monthly
 609 time series of CH_4 lifetime anomalies simulated by STD-F1/F2 and STD-rVolcaoff-F1/F2 experiments. Values over the red lines
 610 represent $\Delta\tau_{CH_4}$.

611 3.4 Model intercomparisons of LFR trends with CMIP6 model outputs

612 The historical lightning trends demonstrated in our study are undoubtedly worth comparing with the results of other chemistry–
 613 climate models or Earth system models. As introduced in Sect. 2.4, for comparison of the simulated LFR trends and variations

614 in our study with those of other CMIP6 models' outputs, we used all available LFR data from the CMIP6 CMIP Historical
615 experiments from CESM2-WACCM (3 ensembles) (Danabasoglu, 2019), GISS-E2-1-G (9 ensembles) (Kelley et al., 2020),
616 and UKESM1-0-LL (18 ensembles) (Tang et al., 2019). Table S1 presents a complete list of the ensemble members we used.
617 It is noteworthy that the LFR data obtained from the three CMIP6 models described earlier are calculated using the CTH
618 scheme. The results of model intercomparisons of LFR trends and variations are displayed in Fig. 15.

619 As ~~illustrated~~displayed in Figs. 15a–15b and Table 6, both the ECMWF-McCAUL and the CTH schemes (STD-F1/F2)
620 simulated almost flat ~~statistically non-significant~~ global lightning trends; (even the trend is estimated to be significant in the
621 case of the CTH scheme (0.03 % yr⁻¹)), but the ensemble mean obtained from another three CMIP6 models exhibit much larger
622 significant increasing global lightning trends (trends from 0.11% yr⁻¹ to 0.25% yr⁻¹). Many reasons underlie the differences in
623 global lightning trends simulated by CHASER in our study and by the three CMIP6 models, including the use of different
624 methods to determine SSTs/sea ice fields. Instead of using a coupled Atmosphere–Ocean general circulation model to calculate
625 SSTs/sea ice fields dynamically in the three CMIP6 models, CHASER uses the prescribed HadISST data (Rayner et al., 2003),
626 which are based on plenty of observational data. Changes in the global mean sea surface temperature anomaly during 1960–
627 2014 (Δ SST) obtained from STD-F1/F2 and CMIP6 model outputs are presented in Table 25. We also used the observation-
628 based Extended Reconstructed SST (ERSST) dataset (Huang et al., 2017) constructed by NOAA to evaluate the Δ SST obtained
629 from different models. The Δ SST calculated from ERSST during 1960–2014 is 0.549°C, which most closely approximates the
630 Δ SST obtained from STD-F1/F2. Considered from the perspective of SSTs/sea ice fields alone, the results (global lightning
631 trends) of our study are expected to be closer to the actual situation.

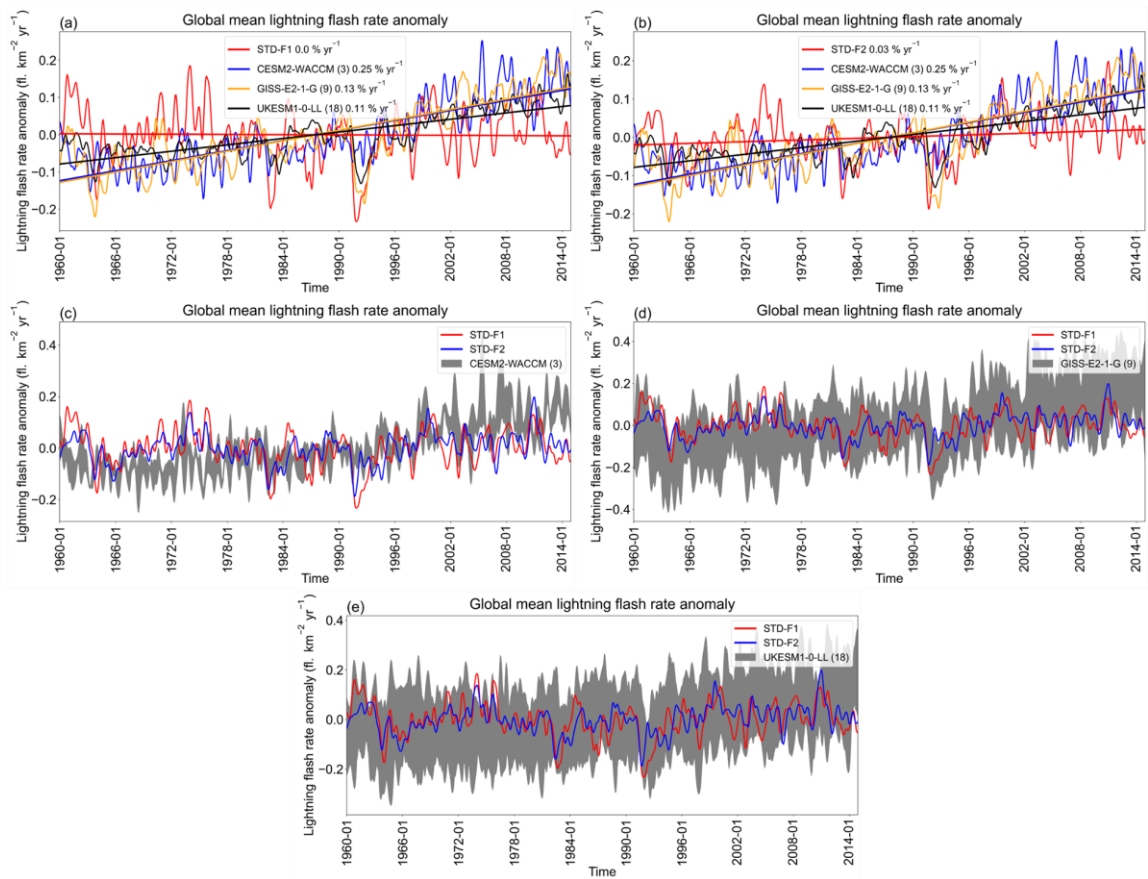
632
633 Actually, the three CMIP6 models simulated stronger global warming during 1960–2014 than CHASER in our study, as
634 displayed in Fig. S7 and Table 5. The CTH scheme is reported to respond positively to simulated global warming (Price and
635 Rind, 1994; Zeng et al., 2008; Hui and Hong, 2013; Banerjee et al., 2014; Krause et al., 2014; Clark et al., 2017). The simulated
636 stronger global warming by the three CMIP6 models is regarded as responsible for differences in simulated global lightning
637 trends between our study and the three CMIP6 models (Figs. 15a–15b and Table 6). We further investigated the sensitivities
638 of the global mean LFR anomaly change to the global mean surface temperature anomaly increase (% °C⁻¹) obtained from
639 CHASER and the three CMIP6 models. The sensitivities in percentage per degree Celsius are presented in Table 25. Overall,
640 even when using the same CTH scheme, the sensitivities (Δ LFR/ Δ TS) simulated by the three CMIP6 models are higher than
641 that simulated by CHASER in our study. This different sensitivity might be partially attributable to the nonlinear relation
642 between lightning response and climate change (Pinto, 2013; Krause et al., 2014). Compared to the CTH scheme, the ECMWF-
643 McCAUL scheme simulated a statistically non-significant negative sensitivity (Δ LFR/ Δ TS), which is attributable to the
644 stronger suppression of positive global lightning trends caused by increases in AeroPEs simulated using the ECMWF-
645 McCAUL scheme.

646

647 **Table 25:** Changes in global mean surface temperature anomaly (ΔTS), global mean sea surface temperature anomaly (ΔSST), global
648 mean lightning flash rate anomaly (ΔLFR), and the rate of change of LFR anomaly corresponding to each degree-Celsius increase
649 in global mean surface temperature anomaly ($\Delta LFR/\Delta TS$) obtained from STD-F1/F2 and CMIP6 model outputs. The change of
650 ΔSST obtained from the ERSST dataset is also shown in this Table. Changes were obtained by calculating the difference between
651 the rightmost and leftmost points of the approximating curve for the 1960–2014 time-series data.

Model/experiment/dataset	ΔTS ($^{\circ}C$)	ΔSST ($^{\circ}C$)	ΔLFR (%)	$\Delta LFR/\Delta TS$ ($\% \text{ } ^{\circ}C^{-1}$)
STD-F1	0.593	0.428	-0.272	-0.46
STD-F2	0.563	0.432	1.497	2.66
CESM2-WACCM	1.245	1.077	13.758	11.05
GISS-E2-1-G	0.810	0.677	7.248	8.95
UKESM1-0-LL	1.141	0.999	5.942	5.21
ERSST	—	0.549	—	—

652
653 Figures 15d–15e affirm that the global lightning variation simulated by our study is basically within the full ensemble range
654 of GISS-E2-1-G and UKESM1-0-LL. After the Pinatubo eruption, as described in Sect. 3.3 of this report, the GISS-E2-1-G
655 and UKESM1-0-LL models also manifest significant suppression of global lightning activities, but the CESM2-WACCM
656 model shows no such phenomenon. The commonalities and differences in global lightning trends and variations found in the
657 model intercomparisons imply that great uncertainties existed in past (1960–2014) global lightning trend simulations. Such
658 uncertainties deserve to be investigated further.



659

660 **Figure 15: Comparisons of simulated global mean LFR anomalies found in our study (CHASER) and found using other CMIP6**
 661 **models. All the figures are created based on the monthly time-series data of global mean LFR anomalies with a 1-D Gaussian**
 662 **(Denosing) filter applied. For CMIP6 models, the ensemble mean is shown as the solid line, and the full ensemble range is shown as**
 663 **grey shading (c–e). Fitting curves and the trends of fitting curves ($\% \text{ yr}^{-1}$) are also given in (a–b).**

664

665 **Table 6: A statistical summary of the trends shown in Figs. 15a–15b by Mann–Kendall rank statistic and Sen’s slope estimator. The**
 666 **time-series data of global mean LFR anomalies were estimated by Mann–Kendall rank statistic and Sen’s slope estimator. The**
 667 **column “Trend” shows whether these are significant trends with the significance set as 5%, as well as the percentage trends in $\%$**
 668 **yr^{-1} estimated by linear regression. The “ p -value” is calculated during Mann-Kendall trend test. “Slope” shows Sen’s slope of trend.**
 669 **Q_{\min} and Q_{\max} respectively denote the lower and upper limits of the 95% confidence interval of Sen’s slope.**

670

<u>Experiment/model</u>	<u>Trend</u>	<u>p-value</u>	<u>Slope</u>	<u>Q_{\min}</u>	<u>Q_{\max}</u>
<u>STD-F1</u>	<u>No trend, 0.0 $\% \text{ yr}^{-1}$</u>	<u>$p > 0.05$</u>	<u>0.0</u>	<u>-0.0001</u>	<u>0.0</u>
<u>STD-F2</u>	<u>Increasing, 0.03 $\% \text{ yr}^{-1}$</u>	<u>$p < 0.01$</u>	<u>0.0001</u>	<u>0.0</u>	<u>0.0001</u>
<u>CESM2-WACCM</u>	<u>Increasing, 0.25 $\% \text{ yr}^{-1}$</u>	<u>$p < 0.01$</u>	<u>0.0004</u>	<u>0.0003</u>	<u>0.0004</u>

<u>GISS-E2-1-G</u>	<u>Increasing, 0.13 % yr⁻¹</u>	<u>$p < 0.01$</u>	<u>0.0004</u>	<u>0.0004</u>	<u>0.0004</u>
<u>UKESM1-0-LL</u>	<u>Increasing, 0.11 % yr⁻¹</u>	<u>$p < 0.01$</u>	<u>0.0002</u>	<u>0.0002</u>	<u>0.0003</u>

671 4 Discussion and Conclusions

672 We used two lightning schemes (the CTH and ECMWF-McCAUL schemes) to study historical (1960–2014) lightning–LNO_x
673 trends and variations and their influencing factors (global warming, increases in AeroPEs, and Pinatubo eruption) within the
674 CHASER (MIROC) chemistry–climate model. The CTH scheme, which is the most widely used lightning scheme,
675 nevertheless lacks a direct physical link with the charging mechanism. The ECMWF-McCAUL scheme is a newly developed
676 process-based/ice-based lightning scheme with a direct physical link to the charging mechanism.

677
678 With only the aerosol radiative effects considered in the lightning–aerosols interaction, both lightning schemes simulated
679 almost flat trends of global mean LFR during 1960–2014. (no trend is detected in the case of the ECMWF-McCAUL scheme,
680 but a slightly significant increasing trend is detected in the case of the CTH scheme). Reportedly, because the aerosol
681 microphysical effects can enhance lightning activities (Yuan et al., 2011; Wang et al., 2018; Liu et al., 2020), our study might
682 underestimate the increasing trend of global mean LFR (our study only considered the aerosol radiative effects in aerosol–
683 lightning interactions). Further research is anticipated, with consideration of the effects of aerosol microphysical effects on
684 long-term lightning trends. Moreover, both lightning schemes manifest that past global warming enhances the historical trend
685 of global mean lightning density toward the positive direction (around 0.03% yr⁻¹ or 3% K⁻¹). However, past increases in
686 AeroPEs exert the opposite effect to the lightning trend (-0.07% yr⁻¹ – -0.04% yr⁻¹). The effects of the increased AeroPEs on
687 the lightning trend only over land regions expand to -0.10% yr⁻¹ – -0.05% yr⁻¹, which implies that the effects are more
688 significant over land regions. We obtained similar results for the historical global LNO_x emissions trend, which indicates that
689 historical global warming and increases in AeroPEs can affect atmospheric chemistry and engender feedback by influencing
690 LNO_x emissions. Although the CTH and ECMWF-McCAUL schemes use different parameters to simulate lightning, both
691 lightning schemes indicate that the enhanced global convective activity under global warming is the main reason for the
692 increase in lightning–LNO_x emissions. In contrast, the increases in AeroPEs have decreased lightning–LNO_x emissions by
693 weakening the convective activity in the lightning hotspots. By analyzing the simulation results on the global map, we also
694 found that the effects of historical global warming and increases in AeroPEs on lightning trends are heterogeneous across
695 different regions. Our results indicate that historical global warming enhances lightning activities within the Arctic region and
696 Japan but suppresses lightning activities around New Zealand and some parts of the Southern Ocean. Both lightning schemes
697 demonstrated that the historical increases in AeroPEs suppress lightning activities in some parts of the Southern Ocean and
698 South America. The ECMWF-McCAUL scheme also suggests that historical increases in AeroPEs suppress lightning activities
699 in some parts of India and China when only the aerosol radiative effects are considered. This finding is plausible because both
700 countries experienced dramatic increases in AeroPEs during 1960–2014 because of rapid economic growth.

701

702 Furthermore, this report is the first describing significant suppression of global lightning activity during the first year after the
703 Pinatubo eruption, which is indicated in both lightning schemes (global lightning activities decreased by up to 18.10%
704 simulated by the ECMWF-McCAUL scheme). This finding is mainly attributable to the Pinatubo eruption weakening of the
705 convective activities within the hotspots of lightning, which in turn decreased Q_{Ra} and middle-level to high-level cumulus
706 cloud fractions in these regions. The simulation results also indicate that the Pinatubo eruption can engender reductions in
707 global LNO_x emissions, which last 2–3 years. However, some uncertainty exists in evaluating magnitude of these reductions
708 (from 1.99% to 8.47% for the annual percentage reduction in our study). The case study of the Pinatubo eruption in our research
709 indicates that other large-scale volcanic eruptions can also engender significant reduction of global lightning activities and
710 global-scale LNO_x emissions.

711

712 Lastly, we compared the global lightning trends demonstrated in our study with the outputs of three CMIP6 models: CESM2-
713 WACCM, GISS-E2-1-G, and UKESM1-0-LL. We used all available LFR data from the CMIP6 CMIP historical experiments
714 from the three models described above. The three CMIP6 models suggest significant increasing trends in historical global
715 lightning activities, which differs from the findings of our study- [in the magnitude of lightning trends](#). Unlike the three CMIP6
716 models which use a coupled Atmosphere–Ocean general circulation model to calculate SSTs/sea ice fields dynamically, our
717 study (CHASER) uses the prescribed HadISST SSTs/sea ice data, which more closely reflect the actual situation. Therefore,
718 we believe that the results (the historical global lightning trends) obtained from our study (CHASER) more closely approximate
719 the actual situation. However, model intercomparisons of global lightning trends still indicate that considerable uncertainties
720 exist in historical (1960–2014) global lightning trend simulations, and that such uncertainties deserve further investigation.

721 **Code availability**

722 The source code for CHASER to reproduce results obtained from this work is obtainable from the repository at
723 <https://doi.org/10.5281/zenodo.5835796> (He et al., 2022a).

724 **Data availability**

725 The LIS/OTD data used for this study are available from <https://ghrc.nsstc.nasa.gov/hydro/?q=LRTS> (last access: 11 January
726 2022). The CMIP6 model outputs (LFR and surface temperature) used for this study are available from
727 <https://aims2.llnl.gov/search> (last access: 1 February 2023). The Extended Reconstructed SST data used for this study are
728 available from <https://www.ncei.noaa.gov/products/extended-reconstructed-sst> (last access: 27 March 2023).

729 **Author contributions**

730 YFH conducted all simulations, interpreted the results, and wrote the manuscript. KS developed the CHASER (MIROC) model
731 code, conceived the presented idea, and supervised the findings of this work and the manuscript preparation.

732 **Competing interests**

733 The authors declare that they have no conflict of interest.

734 **Acknowledgments**

735 This research was supported by the Global Environment Research Fund (S–12 and S–20) of the Ministry of the Environment
736 (MOE), Japan, and JSPS KAKENHI Grant Numbers: JP20H04320, JP19H05669, and JP19H04235. This work was supported
737 by the Japan Science and Technology Agency (JST) Support for Pioneering Research Initiated by the Next Generation
738 (SPRAING), Grant Number JPMJSP2125. The author would like to take this opportunity to thank the “Interdisciplinary
739 Frontier Next-Generation Researcher Program of the Tokai Higher Education and Research System.” The simulations were
740 completed using the supercomputer (NEC SX-Aurora TSUBASA) at NIES (Japan). We thank NASA scientists and staff for
741 providing LIS/OTD lightning observation data. We acknowledge the World Climate Research Programme, which coordinated
742 and promoted CMIP6 through its Working Group on Coupled Modelling. We extend our sincere gratitude to the climate
743 modelling groups for producing and providing their model outputs, to the Earth System Grid Federation (ESGF) for archiving
744 the data and providing free downloads, and to the multiple funding agencies that have supported the CMIP6 as well as the
745 Earth System Grid Federation. We also thank Ms. Do Thi Nhu Ngoc for her assistance in downloading the CMIP6 model
746 outputs.

747 **References**

- 748 Allen, D. J., Pickering, K. E., Bucsela, E., Krotkov, N., and Holzworth, R.: Lightning NO_x Production in the Tropics as
749 Determined Using OMI NO₂ Retrievals and WWLLN Stroke Data, *Journal of Geophysical Research: Atmospheres*, 124,
750 13498–13518, <https://doi.org/10.1029/2018JD029824>, 2019.
- 751 Altaratz, O., Kucienska, B., Kostinski, A., Raga, G. B., and Koren, I.: Global association of aerosol with flash density of
752 intense lightning, *Environ. Res. Lett.*, 12, 114037, <https://doi.org/10.1088/1748-9326/aa922b>, 2017.
- 753 Earle Williams: <https://web.mit.edu/earlerw/www/index.html>, last access: 19 December 2022.
- 754 Arfeuille, F., Luo, B. P., Heckendorn, P., Weisenstein, D., Sheng, J. X., Rozanov, E., Schraner, M., Brönnimann, S., Thomason,
755 L. W., and Peter, T.: Modeling the stratospheric warming following the Mt. Pinatubo eruption: uncertainties in aerosol
756 extinctions, *Atmospheric Chemistry and Physics*, 13, 11221–11234, <https://doi.org/10.5194/acp-13-11221-2013>, 2013.

757 Banerjee, A., Archibald, A. T., Maycock, A. C., Telford, P., Abraham, N. L., Yang, X., Braesicke, P., and Pyle, J. A.: Lightning
758 NO_x, a key chemistry-climate interaction: Impacts of future climate change and consequences for tropospheric oxidising
759 capacity, *Atmospheric Chemistry and Physics*, 14, 9871–9881, <https://doi.org/10.5194/acp-14-9871-2014>, 2014.

760 Boccippio, D. J., Koshak, W. J., and Blakeslee, R. J.: Performance Assessment of the Optical Transient Detector and Lightning
761 Imaging Sensor. Part I: Predicted Diurnal Variability, *Journal of Atmospheric and Oceanic Technology*, 19, 1318–1332,
762 [https://doi.org/10.1175/1520-0426\(2002\)019<1318:PAOTOT>2.0.CO;2](https://doi.org/10.1175/1520-0426(2002)019<1318:PAOTOT>2.0.CO;2), 2002.

763 Boucher, O.: *Atmospheric Aerosols*, Springer Netherlands, Dordrecht, <https://doi.org/10.1007/978-94-017-9649-1>, 2015.

764 Bucsela, E. J., Pickering, K. E., Allen, D. J., Holzworth, R. H., and Krotkov, N. A.: Midlatitude Lightning NO_x Production
765 Efficiency Inferred From OMI and WWLLN Data, *Journal of Geophysical Research: Atmospheres*, 124, 13475–13497,
766 <https://doi.org/10.1029/2019JD030561>, 2019.

767 Cecil, D. J., Buechler, D. E., and Blakeslee, R. J.: Gridded lightning climatology from TRMM-LIS and OTD: Dataset
768 description, *Atmospheric Research*, 135–136, 404–414, <https://doi.org/10.1016/j.atmosres.2012.06.028>, 2014.

769 Cerveny, R. S., Bessemoulin, P., Burt, C. C., Cooper, M. A., Cunjie, Z., Dewan, A., Finch, J., Holle, R. L., Kalkstein, L.,
770 Kruger, A., Lee, T., Martínez, R., Mohapatra, M., Pattanaik, D. R., Peterson, T. C., Sheridan, S., Trewin, B., Tait, A.,
771 and Wahab, M. M. A.: WMO Assessment of Weather and Climate Mortality Extremes: Lightning, Tropical Cyclones,
772 Tornadoes, and Hail, *Weather, Climate, and Society*, 9, 487–497, <https://doi.org/10.1175/WCAS-D-16-0120.1>, 2017.

773 Clark, S. K., Ward, D. S., and Mahowald, N. M.: Parameterization-based uncertainty in future lightning flash density,
774 *Geophysical Research Letters*, 44, 2893–2901, <https://doi.org/10.1002/2017GL073017>, 2017.

775 Cooper, M. A. and Holle, R. L.: Current Global Estimates of Lightning Fatalities and Injuries, in: *Reducing Lightning Injuries*
776 *Worldwide*, edited by: Cooper, M. A. and Holle, R. L., Springer International Publishing, Cham, 65–73,
777 https://doi.org/10.1007/978-3-319-77563-0_6, 2019.

778 Cooray, V., Rahman, M., and Rakov, V.: On the NO_x production by laboratory electrical discharges and lightning, *Journal of*
779 *Atmospheric and Solar-Terrestrial Physics*, 71, 1877–1889, <https://doi.org/10.1016/j.jastp.2009.07.009>, 2009.

780 Danabasoglu, G.: NCAR CESM2-WACCM model output prepared for CMIP6 CMIP historical,
781 <https://doi.org/10.22033/ESGF/CMIP6.10071>, 2019.

782 Danabasoglu, G., Lamarque, J.-F., Bacmeister, J., Bailey, D. A., DuVivier, A. K., Edwards, J., Emmons, L. K., Fasullo, J.,
783 Garcia, R., Gettelman, A., Hannay, C., Holland, M. M., Large, W. G., Lauritzen, P. H., Lawrence, D. M., Lenaerts, J. T.
784 M., Lindsay, K., Lipscomb, W. H., Mills, M. J., Neale, R., Oleson, K. W., Otto-Bliesner, B., Phillips, A. S., Sacks, W.,
785 Tilmes, S., van Kampenhout, L., Vertenstein, M., Bertini, A., Dennis, J., Deser, C., Fischer, C., Fox-Kemper, B., Kay, J.
786 E., Kinnison, D., Kushner, P. J., Larson, V. E., Long, M. C., Mickelson, S., Moore, J. K., Nienhouse, E., Polvani, L.,
787 Rasch, P. J., and Strand, W. G.: The Community Earth System Model Version 2 (CESM2), *Journal of Advances in*
788 *Modeling Earth Systems*, 12, e2019MS001916, <https://doi.org/10.1029/2019MS001916>, 2020.

789 Del Genio, A. D., Yao, M.-S., and Jonas, J.: Will moist convection be stronger in a warmer climate?, *Geophysical Research*
790 *Letters*, 34, <https://doi.org/10.1029/2007GL030525>, 2007.

791 Finney, D. L., Doherty, R. M., Wild, O., Huntrieser, H., Pumphrey, H. C., and Blyth, A. M.: Using cloud ice flux to parametrise
792 large-scale lightning, *Atmospheric Chemistry and Physics*, 14, 12665–12682, [https://doi.org/10.5194/acp-14-12665-](https://doi.org/10.5194/acp-14-12665-2014)
793 2014, 2014.

794 Finney, D. L., Doherty, R. M., Wild, O., Young, P. J., and Butler, A.: Response of lightning NO_x emissions and ozone
795 production to climate change: Insights from the Atmospheric Chemistry and Climate Model Intercomparison Project,
796 *Geophysical Research Letters*, 43, 5492–5500, <https://doi.org/10.1002/2016GL068825>, 2016a.

797 Finney, D. L., Doherty, R. M., Wild, O., and Abraham, N. L.: The impact of lightning on tropospheric ozone chemistry using
798 a new global lightning parametrisation, *Atmospheric Chemistry and Physics*, 16, 7507–7522, [https://doi.org/10.5194/acp-](https://doi.org/10.5194/acp-16-7507-2016)
799 16-7507-2016, 2016b.

800 Finney, D. L., Doherty, R. M., Wild, O., Stevenson, D. S., MacKenzie, I. A., and Blyth, A. M.: A projected decrease in
801 lightning under climate change, *Nature Climate Change*, 8, 210–213, <https://doi.org/10.1038/s41558-018-0072-6>, 2018.

802 Fujibe, F.: Long-term Change in Lightning Mortality and Its Relation to Annual Thunder Days in Japan, *Journal of Natural*
803 *Disaster Science*, 38, 17–29, <https://doi.org/10.2328/jnds.38.17>, 2017.

804 Goodman, S. J., Buechler, D. E., and Wright, P. D.: Lightning/rainfall relationships during COHMEX, NTRS Author
805 Affiliations: NASA Marshall Space Flight Center, Universities Space Research Association NTRS Document ID:
806 19900057799 NTRS Research Center: Legacy CDMS (CDMS), 1990.

807 Goto, D., Nakajima, T., Dai, T., Takemura, T., Kajino, M., Matsui, H., Takami, A., Hatakeyama, S., Sugimoto, N., Shimizu,
808 A., and Ohara, T.: An evaluation of simulated particulate sulfate over East Asia through global model intercomparison,
809 *Journal of Geophysical Research: Atmospheres*, 120, 6247–6270, <https://doi.org/10.1002/2014JD021693>, 2015.

810 Guenther, A. B., Jiang, X., Heald, C. L., Sakulyanontvittaya, T., Duhl, T., Emmons, L. K., and Wang, X.: The Model of
811 Emissions of Gases and Aerosols from Nature version 2.1 (MEGAN2.1): an extended and updated framework for
812 modeling biogenic emissions, *Geosci. Model Dev.*, 5, 1471–1492, <https://doi.org/10.5194/gmd-5-1471-2012>, 2012.

813 Ha, P. T. M., Matsuda, R., Kanaya, Y., Taketani, F., and Sudo, K.: Effects of heterogeneous reactions on tropospheric
814 chemistry: A global simulation with the chemistry-climate model CHASER V4.0, *Geoscientific Model Development*, 14,
815 3813–3841, <https://doi.org/10.5194/gmd-14-3813-2021>, 2021.

816 He, Y., Hoque, M. S. H., and Sudo, K.: Introducing new lightning schemes into the CHASER (MIROC) chemistry climate
817 model, [code], Zenodo, <https://doi.org/10.5281/zenodo.5835796>, 2022a.

818 He, Y., Hoque, H. M. S., and Sudo, K.: Introducing new lightning schemes into the CHASER (MIROC) chemistry–climate
819 model, *Geoscientific Model Development*, 15, 5627–5650, <https://doi.org/10.5194/GMD-15-5627-2022>, 2022b.

820 Hoesly, R. M., Smith, S. J., Feng, L., Klimont, Z., Janssens-Maenhout, G., Pitkanen, T., Seibert, J. J., Vu, L., Andres, R. J.,
821 Bolt, R. M., Bond, T. C., Dawidowski, L., Kholod, N., Kurokawa, J., Li, M., Liu, L., Lu, Z., Moura, M. C. P., O’Rourke,
822 P. R., and Zhang, Q.: Historical (1750–2014) anthropogenic emissions of reactive gases and aerosols from the
823 Community Emissions Data System (CEDS), *Geosci. Model Dev.*, 11, 369–408, [https://doi.org/10.5194/gmd-11-369-](https://doi.org/10.5194/gmd-11-369-2018)
824 2018, 2018.

825 Huang, B., Thorne, P. W., Banzon, V. F., Boyer, T., Chepurin, G., Lawrimore, J. H., Menne, M. J., Smith, T. M., Vose, R. S.,
826 and Zhang, H.-M.: Extended Reconstructed Sea Surface Temperature, Version 5 (ERSSTv5): Upgrades, Validations, and
827 Intercomparisons, *Journal of Climate*, 30, 8179–8205, <https://doi.org/10.1175/JCLI-D-16-0836.1>, 2017.

828 Hui, J. and Hong, L.: Projected Changes in NO_x Emissions from Lightning as a Result of 2000–2050 Climate Change,
829 *Atmospheric and Oceanic Science Letters*, 6, 284–289, <https://doi.org/10.3878/j.issn.1674-2834.13.0042>, 2013.

830 Hussain, Md. and Mahmud, I.: pyMannKendall: a python package for non parametric Mann Kendall family of trend tests.,
831 *Journal of Open Source Software*, 4, 1556, <https://doi.org/10.21105/joss.01556>, 2019.

832 Ito, A. and Inatomi, M.: Water-use efficiency of the terrestrial biosphere: A model analysis focusing on interactions between
833 the global carbon and water cycles, *Journal of Hydrometeorology*, 13, 681–694, <https://doi.org/10.1175/JHM-D-10-05034.1>, 2012.

835 Jensen, J. D., Thurman, J., and Vincent, A. L.: Lightning Injuries, in: StatPearls, StatPearls Publishing, Treasure Island (FL),
836 2022.

837 Kaufman, Y. J., Tanré, D., Holben, B. N., Mattoo, S., Remer, L. A., Eck, T. F., Vaughan, J., and Chatenet, B.: Aerosol
838 Radiative Impact on Spectral Solar Flux at the Surface, Derived from Principal-Plane Sky Measurements, *Journal of the*
839 *Atmospheric Sciences*, 59, 635–646, [https://doi.org/10.1175/1520-0469\(2002\)059<0635:ARIOSS>2.0.CO;2](https://doi.org/10.1175/1520-0469(2002)059<0635:ARIOSS>2.0.CO;2), 2002.

840 Kelley, M., Schmidt, G. A., Nazarenko, L. S., Bauer, S. E., Ruedy, R., Russell, G. L., Ackerman, A. S., Aleinov, I., Bauer, M.,
841 Bleck, R., Canuto, V., Cesana, G., Cheng, Y., Clune, T. L., Cook, B. I., Cruz, C. A., Del Genio, A. D., Elsaesser, G. S.,
842 Faluvegi, G., Kiang, N. Y., Kim, D., Lacis, A. A., Leboissetier, A., LeGrande, A. N., Lo, K. K., Marshall, J., Matthews,
843 E. E., McDermid, S., Mezuman, K., Miller, R. L., Murray, L. T., Oinas, V., Orbe, C., García-Pando, C. P., Perlwitz, J.
844 P., Puma, M. J., Rind, D., Romanou, A., Shindell, D. T., Sun, S., Tausnev, N., Tsigaridis, K., Tselioudis, G., Weng, E.,
845 Wu, J., and Yao, M.-S.: GISS-E2.1: Configurations and Climatology, *Journal of Advances in Modeling Earth Systems*,
846 12, e2019MS002025, <https://doi.org/10.1029/2019MS002025>, 2020.

847 Koren, I., Kaufman, Y. J., Remer, L. A., and Martins, J. V.: Measurement of the Effect of Amazon Smoke on Inhibition of
848 Cloud Formation, *Science*, 303, 1342–1345, <https://doi.org/10.1126/science.1089424>, 2004.

849 Koren, I., Martins, J. V., Remer, L. A., and Afargan, H.: Smoke Invigoration Versus Inhibition of Clouds over the Amazon,
850 *Science*, 321, 946–949, <https://doi.org/10.1126/science.1159185>, 2008.

851 Krause, A., Kloster, S., Wilkenskjeld, S., and Paeth, H.: The sensitivity of global wildfires to simulated past, present, and
852 future lightning frequency, *Journal of Geophysical Research: Biogeosciences*, 119, 312–322,
853 <https://doi.org/10.1002/2013JG002502>, 2014.

854 Labrador, L. J., von Kuhlmann, R., and Lawrence, M. G.: The effects of lightning-produced NO_x and its vertical distribution
855 on atmospheric chemistry: sensitivity simulations with MATCH-MPIC, *Atmospheric Chemistry and Physics*, 5, 1815–
856 1834, <https://doi.org/10.5194/acp-5-1815-2005>, 2005.

857 Lal, D. M., Ghude, S. D., Mahakur, M., Waghmare, R. T., Tiwari, S., Srivastava, M. K., Meena, G. S., and Chate, D. M.:
858 Relationship between aerosol and lightning over Indo-Gangetic Plain (IGP), India, *Clim Dyn*, 50, 3865–3884,
859 <https://doi.org/10.1007/s00382-017-3851-2>, 2018.

860 Li, Z., Guo, J., Ding, A., Liao, H., Liu, J., Sun, Y., Wang, T., Xue, H., Zhang, H., and Zhu, B.: Aerosol and boundary-layer
861 interactions and impact on air quality, *National Science Review*, 4, 810–833, <https://doi.org/10.1093/nsr/nwx117>, 2017.

862 Liaskos, C. E., Allen, D. J., and Pickering, K. E.: Sensitivity of tropical tropospheric composition to lightning NO_x production
863 as determined by replay simulations with GEOS-5, *Journal of Geophysical Research*, 120, 8512–8534,
864 <https://doi.org/10.1002/2014JD022987>, 2015.

865 Liu, Y., Guha, A., Said, R., Williams, E., Lapierre, J., Stock, M., and Heckman, S.: Aerosol Effects on Lightning
866 Characteristics: A Comparison of Polluted and Clean Regimes, *Geophysical Research Letters*, 47, e2019GL086825,
867 <https://doi.org/10.1029/2019GL086825>, 2020.

868 Lopez, P.: A lightning parameterization for the ECMWF integrated forecasting system, *Monthly Weather Review*, 144, 3057–
869 3075, <https://doi.org/10.1175/MWR-D-16-0026.1>, 2016.

870 Macias Fauria, M. and Johnson, E. A.: Large-scale climatic patterns control large lightning fire occurrence in Canada and
871 Alaska forest regions, *Journal of Geophysical Research: Biogeosciences*, 111, <https://doi.org/10.1029/2006JG000181>,
872 2006.

873 Mallick, C., Hazra, A., Saha, S. K., Chaudhari, H. S., Pokhrel, S., Konwar, M., Dutta, U., Mohan, G. M., and Vani, K. G.:
874 Seasonal Predictability of Lightning Over the Global Hotspot Regions, *Geophysical Research Letters*, 49,
875 e2021GL096489, <https://doi.org/10.1029/2021GL096489>, 2022.

876 Manabe, S. and Wetherald, R. T.: The Effects of Doubling the CO₂ Concentration on the climate of a General Circulation
877 Model, *Journal of the Atmospheric Sciences*, 32, 3–15, [https://doi.org/10.1175/1520-0469\(1975\)032<0003:TEODTC>2.0.CO;2](https://doi.org/10.1175/1520-0469(1975)032<0003:TEODTC>2.0.CO;2), 1975.

879 NOAA National Centers for Environmental Information (NCEI), Climate at a Glance: Global Time Series, published June
880 2023, retrieved on January 10, 2023 from https://www.ncei.noaa.gov/access/monitoring/climate-at-a-glance/global/time-series/globe/land_ocean/3/8/1880-2020.

882 van Marle, M. J. E., Kloster, S., Magi, B. I., Marlon, J. R., Daniiau, A.-L., Field, R. D., Arneth, A., Forrest, M., Hantson, S.,
883 Kehrwald, N. M., Knorr, W., Lasslop, G., Li, F., Mangeon, S., Yue, C., Kaiser, J. W., and van der Werf, G. R.: Historic
884 global biomass burning emissions for CMIP6 (BB4CMIP) based on merging satellite observations with proxies and fire
885 models (1750–2015), *Geosci. Model Dev.*, 10, 3329–3357, <https://doi.org/10.5194/gmd-10-3329-2017>, 2017.

886 McCaul, E. W., Goodman, S. J., LaCasse, K. M., and Cecil, D. J.: Forecasting lightning threat using cloud-resolving model
887 simulations, *Weather and Forecasting*, 24, 709–729, <https://doi.org/10.1175/2008WAF2222152.1>, 2009.

888 Meinshausen, M., Vogel, E., Nauels, A., Lorbacher, K., Meinshausen, N., Etheridge, D. M., Fraser, P. J., Montzka, S. A.,
889 Rayner, P. J., Trudinger, C. M., Krummel, P. B., Beyerle, U., Canadell, J. G., Daniel, J. S., Enting, I. G., Law, R. M.,
890 Lunder, C. R., O’Doherty, S., Prinn, R. G., Reimann, S., Rubino, M., Velders, G. J. M., Vollmer, M. K., Wang, R. H. J.,

891 and Weiss, R.: Historical greenhouse gas concentrations for climate modelling (CMIP6), Geoscientific Model
892 Development, 10, 2057–2116, <https://doi.org/10.5194/gmd-10-2057-2017>, 2017.

893 Miller, R. L., Schmidt, G. A., Nazarenko, L. S., Tausnev, N., Bauer, S. E., DelGenio, A. D., Kelley, M., Lo, K. K., Ruedy, R.,
894 Shindell, D. T., Aleinov, I., Bauer, M., Bleck, R., Canuto, V., Chen, Y., Cheng, Y., Clune, T. L., Faluvegi, G., Hansen,
895 J. E., Healy, R. J., Kiang, N. Y., Koch, D., Lacis, A. A., LeGrande, A. N., Lerner, J., Menon, S., Oinas, V., Pérez García-
896 Pando, C., Perlwitz, J. P., Puma, M. J., Rind, D., Romanou, A., Russell, G. L., Sato, M., Sun, S., Tsigaridis, K., Unger,
897 N., Voulgarakis, A., Yao, M.-S., and Zhang, J.: CMIP5 historical simulations (1850–2012) with GISS ModelE2, Journal
898 of Advances in Modeling Earth Systems, 6, 441–478, <https://doi.org/10.1002/2013MS000266>, 2014.

899 Murray, L. T.: Lightning NO_x and Impacts on Air Quality, Current Pollution Reports, 2, 115–133,
900 <https://doi.org/10.1007/s40726-016-0031-7>, 2016.

901 Ott, L. E., Pickering, K. E., Stenichkov, G. L., Allen, D. J., DeCaria, A. J., Ridley, B., Lin, R. F., Lang, S., and Tao, W. K.:
902 Production of lightning NO_x and its vertical distribution calculated from three-dimensional cloud-scale chemical transport
903 model simulations, Journal of Geophysical Research Atmospheres, 115, 4301, <https://doi.org/10.1029/2009JD011880>,
904 2010.

905 Pinto, O.: Lightning and climate: A review, in: 2013 International Symposium on Lightning Protection (XII SIPDA), 2013
906 International Symposium on Lightning Protection (XII SIPDA), 402–404, <https://doi.org/10.1109/SIPDA.2013.6729250>,
907 2013.

908 Price, C. and Rind, D.: A simple lightning parameterization for calculating global lightning distributions, Journal of
909 Geophysical Research, 97, 9919–9933, <https://doi.org/10.1029/92JD00719>, 1992.

910 Price, C. and Rind, D.: What determines the cloud-to-ground lightning fraction in thunderstorms?, Geophysical Research
911 Letters, 20, 463–466, <https://doi.org/10.1029/93GL00226>, 1993.

912 Price, C. and Rind, D.: Possible implications of global climate change on global lightning distributions and frequencies, Journal
913 of Geophysical Research, 99, 823–833, <https://doi.org/10.1029/94jd00019>, 1994.

914 Rayner, N. A., Parker, D. E., Horton, E. B., Folland, C. K., Alexander, L. V., Rowell, D. P., Kent, E. C., and Kaplan, A.:
915 Global analyses of sea surface temperature, sea ice, and night marine air temperature since the late nineteenth century,
916 Journal of Geophysical Research: Atmospheres, 108, <https://doi.org/10.1029/2002jd002670>, 2003.

917 Ridley, B. A., Pickering, K. E., and Dye, J. E.: Comments on the parameterization of lightning-produced NO in global
918 chemistry-transport models, Atmospheric Environment, 39, 6184–6187, <https://doi.org/10.1016/j.atmosenv.2005.06.054>,
919 2005.

920 Romps, D. M.: Evaluating the Future of Lightning in Cloud-Resolving Models, Geophysical Research Letters, 46, 14863–
921 14871, <https://doi.org/10.1029/2019GL085748>, 2019.

922 Romps, D. M., Seeley, J. T., Vollaro, D., and Molinari, J.: Projected increase in lightning strikes in the united states due to
923 global warming, Science, 346, 851–854, <https://doi.org/10.1126/science.1259100>, 2014.

924 Sato, M., Hansen, J. E., McCormick, M. P., and Pollack, J. B.: Stratospheric aerosol optical depths, 1850–1990, *Journal of*
925 *Geophysical Research: Atmospheres*, 98, 22987–22994, <https://doi.org/10.1029/93JD02553>, 1993.

926 Saunders, C. P. R., Keith, W. D., and Mitzewa, R. P.: The effect of liquid water on thunderstorm charging, *Journal of*
927 *Geophysical Research: Atmospheres*, 96, 11007–11017, <https://doi.org/10.1029/91JD00970>, 1991.

928 Schumann, U. and Huntrieser, H.: The global lightning-induced nitrogen oxides source, *Atmospheric Chemistry and Physics*,
929 7, 3823–3907, <https://doi.org/10.5194/acp-7-3823-2007>, 2007.

930 Sekiguchi, M. and Nakajima, T.: A k-distribution-based radiation code and its computational optimization for an atmospheric
931 general circulation model, *Journal of Quantitative Spectroscopy and Radiative Transfer*, 109, 2779–2793,
932 <https://doi.org/10.1016/j.jqsrt.2008.07.013>, 2008.

933 Sellar, A. A., Jones, C. G., Mulcahy, J. P., Tang, Y., Yool, A., Wiltshire, A., O’Connor, F. M., Stringer, M., Hill, R., Palmieri,
934 J., Woodward, S., de Mora, L., Kuhlbrodt, T., Rumbold, S. T., Kelley, D. I., Ellis, R., Johnson, C. E., Walton, J., Abraham,
935 N. L., Andrews, M. B., Andrews, T., Archibald, A. T., Berthou, S., Burke, E., Blockley, E., Carslaw, K., Dalvi, M.,
936 Edwards, J., Folberth, G. A., Gedney, N., Griffiths, P. T., Harper, A. B., Hendry, M. A., Hewitt, A. J., Johnson, B., Jones,
937 A., Jones, C. D., Keeble, J., Liddicoat, S., Morgenstern, O., Parker, R. J., Predoi, V., Robertson, E., Siahahaan, A., Smith,
938 R. S., Swaminathan, R., Woodhouse, M. T., Zeng, G., and Zerroukat, M.: UKESM1: Description and Evaluation of the
939 U.K. Earth System Model, *Journal of Advances in Modeling Earth Systems*, 11, 4513–4558,
940 <https://doi.org/10.1029/2019MS001739>, 2019.

941 Shi, Z., Wang, H., Tan, Y., Li, L., and Li, C.: Influence of aerosols on lightning activities in central eastern parts of China,
942 *Atmospheric Science Letters*, 21, e957, <https://doi.org/10.1002/asl.957>, 2020.

943 Soden, B. J., Wetherald, R. T., Stenchikov, G. L., and Robock, A.: Global Cooling After the Eruption of Mount Pinatubo: A
944 Test of Climate Feedback by Water Vapor, *Science*, 296, 727–730, <https://doi.org/10.1126/science.296.5568.727>, 2002.

945 Sudo, K. and Akimoto, H.: Global source attribution of tropospheric ozone: Long-range transport from various source regions,
946 *Journal of Geophysical Research Atmospheres*, 112, <https://doi.org/10.1029/2006JD007992>, 2007.

947 Sudo, K., Takahashi, M., Kurokawa, J. I., and Akimoto, H.: CHASER: A global chemical model of the troposphere 1. Model
948 description, *Journal of Geophysical Research Atmospheres*, 107, ACH 7-1-ACH 7-20,
949 <https://doi.org/10.1029/2001JD001113>, 2002.

950 T., S., A., M., Anttila, P., Ruoho-Airola, T., and T, A.: Detecting Trends of Annual Values of Atmospheric Pollutants by the
951 Mann-Kendall Test and Sen’s Slope Estimates the Excel Template Application MAKESENS, *Publications on Air Quality*,
952 31, 2002.

953 Takemura, T., Egashira, M., Matsuzawa, K., Ichijo, H., O’Ishi, R., and Abe-Ouchi, A.: A simulation of the global distribution
954 and radiative forcing of soil dust aerosols at the Last Glacial Maximum, *Atmospheric Chemistry and Physics*, 9, 3061–
955 3073, <https://doi.org/10.5194/acp-9-3061-2009>, 2009.

956 Tan, Y. B., Peng, L., Shi, Z., and Chen, H. R.: Lightning flash density in relation to aerosol over Nanjing (China), *Atmospheric*
957 *Research*, 174–175, 1–8, <https://doi.org/10.1016/j.atmosres.2016.01.009>, 2016.

958 Tang, Y., Rumbold, S., Ellis, R., Kelley, D., Mulcahy, J., Sellar, A., Walton, J., and Jones, C.: MOHC UKESM1.0-LL model
959 output prepared for CMIP6 CMIP historical, <https://doi.org/10.22033/ESGF/CMIP6.6113>, 2019.

960 Tost, H.: Chemistry-climate interactions of aerosol nitrate from lightning, *Atmospheric Chemistry and Physics*, 17, 1125–1142,
961 <https://doi.org/10.5194/acp-17-1125-2017>, 2017.

962 Veraverbeke, S., Finney, D., Werf, G. van der, Wees, D. van, Xu, W., and Jones, M.: Global attribution of anthropogenic and
963 lightning fires, *Copernicus Meetings*, <https://doi.org/10.5194/egusphere-egu22-1160>, 2022.

964 Wang, Q., Li, Z., Guo, J., Zhao, C., and Cribb, M.: The climate impact of aerosols on the lightning flash rate: Is it detectable
965 from long-term measurements?, *Atmospheric Chemistry and Physics*, 18, 12797–12816, [https://doi.org/10.5194/acp-18-](https://doi.org/10.5194/acp-18-12797-2018)
966 [12797-2018](https://doi.org/10.5194/acp-18-12797-2018), 2018.

967 Wang, Y., Wan, Q., Meng, W., Liao, F., Tan, H., and Zhang, R.: Long-term impacts of aerosols on precipitation and lightning
968 over the Pearl River Delta megacity area in China, *Atmospheric Chemistry and Physics*, 11, 12421–12436,
969 <https://doi.org/10.5194/acp-11-12421-2011>, 2011.

970 Watanabe, S., Hajima, T., Sudo, K., Nagashima, T., Takemura, T., Okajima, H., Nozawa, T., Kawase, H., Abe, M., Yokohata,
971 T., Ise, T., Sato, H., Kato, E., Takata, K., Emori, S., and Kawamiya, M.: MIROC-ESM 2010: Model description and
972 basic results of CMIP5-20c3m experiments, *Geoscientific Model Development*, 4, 845–872,
973 <https://doi.org/10.5194/gmd-4-845-2011>, 2011.

974 Wild, O.: Modelling the global tropospheric ozone budget: exploring the variability in current models, *Atmospheric Chemistry*
975 *and Physics*, 7, 2643–2660, <https://doi.org/10.5194/acp-7-2643-2007>, 2007.

976 Williams, E. R., Weber, M. E., and Orville, R. E.: The relationship between lightning type and convective state of
977 thunderclouds, *Journal of Geophysical Research: Atmospheres*, 94, 13213–13220,
978 <https://doi.org/10.1029/JD094iD11p13213>, 1989.

979 Yang, X., Yao, Z., Li, Z., and Fan, T.: Heavy air pollution suppresses summer thunderstorms in central China, *Journal of*
980 *Atmospheric and Solar-Terrestrial Physics*, 95–96, 28–40, <https://doi.org/10.1016/j.jastp.2012.12.023>, 2013.

981 Yuan, T., Remer, L. A., Pickering, K. E., and Yu, H.: Observational evidence of aerosol enhancement of lightning activity and
982 convective invigoration, *Geophysical Research Letters*, 38, 4701, <https://doi.org/10.1029/2010GL046052>, 2011.

983 Zeng, G., Pyle, J. A., and Young, P. J.: Impact of climate change on tropospheric ozone and its global budgets, *Atmospheric*
984 *Chemistry and Physics*, 8, 369–387, <https://doi.org/10.5194/acp-8-369-2008>, 2008.

985 Zhao, P., Zhou, Y., Xiao, H., Liu, J., Gao, J., and Ge, F.: Total Lightning Flash Activity Response to Aerosol over China Area,
986 *Atmosphere*, 8, 26, <https://doi.org/10.3390/atmos8020026>, 2017.

987 Zhao, P., Li, Z., Xiao, H., Wu, F., Zheng, Y., Cribb, M. C., Jin, X., and Zhou, Y.: Distinct aerosol effects on cloud-to-ground
988 lightning in the plateau and basin regions of Sichuan, Southwest China, *Atmospheric Chemistry and Physics*, 20, 13379–
989 [13397](https://doi.org/10.5194/acp-20-13379-2020), <https://doi.org/10.5194/acp-20-13379-2020>, 2020.

990
991